Accepted for publication in the ApJ
Preprint typeset using LaTeX style emulateapj v. 5/2/11

arXiv:1304.3899v1 [astro-ph.CO] 14 Apr 2013

STAR FORMATION IN NUCLEAR RINGS OF BARRED GALAXIES

Woo-Young Seo and Woong-Tae Kim
Center for the Exploration of the Origin of the Universe (CEOU), Astronomy Program, Department of Physics & Astronomy, Seoul National University,
Seoul 151-742, Republic of Korea and
FPRD, Department of Physics & Astronomy, Seoul National University, Seoul 151-742, Republic of Korea

Accepted for publication in the ApJ

ABSTRACT

Nuclear rings in barred galaxies are sites of active star formation. We use hydrodynamic simulations to study temporal and spatial behavior of star formation occurring in nuclear rings of barred galaxies where radial gas inflows are triggered solely by a bar potential. The star formation recipes include a density threshold, an efficiency, conversion of gas to star particles, and delayed momentum feedback via supernova explosions. We find that star formation rate (SFR) in a nuclear ring is roughly equal to the mass inflow rate to the ring, while it has a weak dependence on the total gas mass in the ring. The SFR typically exhibits a strong primary burst followed by weak secondary bursts before declining to very small values. The primary burst is associated with the rapid gas infall to the ring due to the bar growth, while the secondary bursts are caused by re-infall of the ejected gas from the primary burst. While star formation in observed rings persists episodically over a few Gyr, the duration of active star formation in our models lasts for only about a half of the bar growth time, suggesting that the bar potential alone is unlikely responsible for gas supply to the rings. When the SFR is low, most star formation occurs at the contact points between the ring and the dust lanes, leading to an azimuthal age gradient of young star clusters. When the SFR is large, on the other hand, star formation is randomly distributed over the whole circumference of the ring, resulting in no apparent azimuthal age gradient. Since the ring shrinks in size with time, star clusters also exhibit a radial age gradient, with younger clusters found closer to the ring. The cluster mass function is well described by a power law, with a slope depending on the SFR. Giant gas clouds in the rings have supersonic internal velocity dispersions and are gravitationally bound.

Subject headings: galaxies: ISM — galaxies: kinematics and dynamics — galaxies: nuclei — galaxies: spiral — ISM: general — shock waves — stars: formation

1. INTRODUCTION

Nuclear rings in barred galaxies are sites of intense star formation (e.g., Burbidge & Burbidge 1960; Sandage 1961; Phillips 1996; Buta & Combes 1996; Knapen et al. 2006; Mazzuca et al. 2008; Comerón et al. 2010; Sandstrom et al. 2010; Mazzuca et al. 2011; Hsieh et al. 2011). These rings are thought to form as a result of nonlinear interactions of gas with a non-axisymmetric bar potential (e.g., Combes & Gerin 1985; Shlosman et al. 1990; Athanassoula 1992; Heller & Shlosman 1994; Knapen et al. 1995; Buta & Combes 1996; Combes 2001; Piner et al. 1995; Regan & Teuben 2003). Due to the bar torque, the gas readily forms dust-lane shocks in the bar region and flows inward along the dust lanes. The inflowing gas speeds up gradually in the azimuthal direction as it moves inward, and shapes into a ring very close to the galaxy center (e.g., Kim et al. 2012a). Consequently, nuclear rings have very large surface densities and short dynamical time scales, capable of triggering starburst activity.

There are some important observational results that may provide clues as to how star formation occurs in the nuclear rings. First of all, observations indicate that the star formation rate (SFR) in the nuclear rings appears to vary with time, and differs considerably from galaxy to galaxy. Analyses of various population synthesis models for a sample of galaxies reveal that the strength of observed emission lines from the nuclear rings is best described by multiple starburst activities over the last 0.5 Gyr or so, rather than by a constant star formation rate (e.g., Allard et al. 2006; Sarzi et al. 2007). For 22 nuclear rings, Mazzuca et al. (2008) found that the present SFRs are widely distributed in the range 0.1–10 $M_\odot$ yr^{-1}. It appears that the SFR is largely insensitive to the total molecular mass in a ring, but can be strongly affected by the bar strength. For instance, the ring in a strongly-barred galaxy NGC 4314 has a relatively low SFR at ~ 0.1 $M_\odot$ yr^{-1} (Benedict et al. 2002), which is about an order of magnitude smaller than that in a weakly-barred galaxy NGC 1326 (Buta et al. 2000), although the total molecular mass contained in the ring is within a factor of two. In fact, the SFRs given in Mazzuca et al. (2008) combined with the bar strength presented by Comerón et al. (2010) show that strongly-barred galaxies tend to have a very small SFR in the rings, while weakly-barred galaxies have a wide range of the SFRs.

Second, based on the spatial distributions of star-forming regions in nuclear rings, Böker et al. (2008) proposed two models of star formation: "popcorn" and "pearls on a string" models (see also Sandstrom et al. 2010). In the first popcorn model, star formation occurs in dense clumps that are randomly distributed along a nuclear ring. This type of star formation, presum-

seowy@astro.snu.ac.kr, wkim@astro.snu.ac.kr

ably caused by gravitational instability of the ring itself (Elmegreen 1994), does not produce a systematic gradient in the ages of young star clusters along the azimuthal direction (see also, e.g., Benedict et al. 2002; Brandle et al. 2012). In the second pearls-on-a-string model, on the other hand, star formation takes place preferentially at the contact points between a ring and dust lanes. This may happen because gas clouds with the largest densities are usually placed at the contact points due to orbit crowding (e.g., Kenney et al. 1992; Reynaud & Downes 1997; Kohno et al. 1999; Hsieh et al. 2011). Since star clusters age as they orbit along the ring, this model naturally predicts a bipolar azimuthal age gradient of star clusters starting from the contact points (see also, e.g., Ryder et al. 2001; Allard et al. 2006; Mazzuca et al. 2008; Böker et al. 2008; Ryder et al. 2010; van der Laan et al 2013). Mazzuca et al. (2008) found that $\sim 50\%$ of the nuclear rings in their sample galaxies show azimuthal age gradients and that such galaxies have, on average, a larger value of the mean SFR than those without noticeable age gradients.

Another interesting observational result concerns radial locations of star clusters relative to the nuclear rings. In some galaxies such as NGC 1512 (Maoz et al. 2001) and NGC 4314 (Benedict et al. 2002), young star clusters are located at larger radii than the dense gas of nuclear rings. Martini et al. (2003) also reported that out of 123 barred galaxies in their sample, eight galaxies have strong nuclear spirals, all of which have star-forming regions outside the rings. By analyzing multi-waveband HST archive data of NGC 1672, Jang & Lee (2013) recently identified hundreds of young and old star clusters with ages in the range $\sim 1 - 10^3$ Myr. They found that the clusters in the nuclear regions exhibit a systematic positive radial age gradient, such that older clusters tend to be located at larger galactocentric radii, farther away from the ring. Proposed mechanisms for the radial age gradient include the decrease in the ring size due to angular momentum loss (Regan & Teuben 2003) and migration of clusters due to tidal interactions with the ring (van de Ven & Chang 2009).

Numerical simulations have been a powerful tool to study formation and evolution of bar substructures such as dust lanes, nuclear rings, and nuclear spirals (e.g., Sanders & Huntley 1976; Athanassoula 1992; Piner et al. 1995; Englmaier & Gerhard 1997; Patsis & Athanassoula 2000; Maciejewski et al. 2002; Regan & Teuben 2003, 2004; Ann & Thakur 2005; Thakur et al. 2009; Kim et al. 2012a,b). In particular, Athanassoula (1992) showed that dust lanes are shocks formed at the downstream side from the bar major axis. Dust lanes tend to be shorter and located closer to the bar major axis as the gas sound speed increases (Englmaier & Gerhard 1997; Patsis & Athanassoula 2000; Kim et al. 2012a).

Very recently, Kim et al. (2012b, hereafter Paper I) ran various models with differing bar strength and demonstrated that nuclear rings form not by resonant interactions of the gas with the bar potential, as was previously thought, but instead by the centrifugal barrier that the inflowing gas with non-vanishing angular momentum cannot overcome. According to this idea, a more massive bar forms stronger dust-lane shocks which remove angular momentum more efficiently from the gas, so that the inflowing gas is able to move inward closer to the galaxy center, forming a smaller nuclear ring. This turns out entirely consistent with the observational result of Comerón et al. (2010) that "stronger bars host smaller rings". Magnetic stress at the dust lanes takes away angular momentum additionally, leading to an even smaller ring compared to the unmagnetized counterpart (Kim & Stone 2012). Paper I also showed that nuclear spirals that form inside nuclear rings unwind with time due to the nonlinear effect (Lee & Goodman 1999), with an unwinding rate higher for a stronger bar. Thus, the probability of having more tightly wound spirals is larger for galaxies with a weaker bar, consistent with the observational result of Peeples & Martini (2006).

While the numerical studies mentioned above are useful to understand gas dynamics in the central regions of barred galaxies, they are without self-gravity and/or prescriptions for star formation. There have been only a few numerical studies that considered star formation in nuclear rings in a self-consistent way. Heller & Shlosman (1994) studied star formation in galactic disks that are unstable to bar formation. Using a smoothed particle hydrodynamics (SPH) combined with N-body method, they found that star formation in barred galaxies occurs episodically, with a time scale of ~ 10 Myr, and that the associated SFR is well correlated with the mass accretion rate to the central black hole (BH). These were confirmed by Knapen et al. (1995) who also found that turbulence driven by star formation tends to widen nuclear rings. Friedli & Benz (1995) used another SPH+N-body method to run various models with differing parameters, finding that star formation in the nuclear regions first experiences a burst phase before entering a quiescent phase (see also Martin & Friedli 1997). Since these authors employed a small number ($\sim 10^4$) of gas particles in their models, however, they were unable to resolve the nuclear regions well. Kim et al. (2011) ran SPH simulations for star formation specific to the central molecular zone in the Milky Way. While Dobbs & Pringle (2010) studied cluster age distributions in spiral and barred galaxies, their results were based on SPH simulations that did not consider star formation and feedback.

In this paper, we extend Paper I by including self-gravity and a prescription for star formation feedback. We focus on temporal and spatial distributions of star formation occurring in nuclear rings of strongly-barred galaxies. Unlike the previous SPH simulations with star formation, our models use a grid-based, cylindrical code with high spatial resolution in the central regions. We also allow for time delays between star formation and feedback, which is crucial to study age gradients of star clusters that form in nuclear rings. Our main objectives are to address important questions such as what controls the SFR in the nuclear rings and what are responsible for the presence (or absence) of the age gradients of star clusters in the rings, mentioned above.

We take a simple galaxy model in which a self-gravitating gaseous disk with either uniform or exponential density distribution is placed under the influence of a non-axisymmetric bar potential. We implement a stochastic prescription for star formation that takes allowance for a threshold density as well as a star formation efficiency. Star formation feedback is treated only through direct momentum injections from supernova (SN) explosions occurring 10 Myr after star formation events. By considering an isothermal equation of state, we do not consider gas cooling and heating, and radiative feedback, which may be important in regulating star formation in disk galaxies (e.g., Ostriker et al. 2010; Ostriker & Shetty 2011; Kim et al. 2011; Shetty & Ostriker 2012). In our models, the bar potential is turned on slowly over time, which not only represents a situation where the bar forms and grows but also helps avoid abrupt gas responses. In each model, we measure the SFR in the ring and study its dependence on various quantities such as the gas mass in the ring, mass inflow rates to the central regions, bar growth time, etc. We also explore temporal and spatial variations of star-forming regions and their connection to the SFR. In addition, we study physical properties of star clusters and gas clouds in the rings and compare them with observational results available.

We remark on a few important limitations of our models from the outset. First of all, our gaseous disks are two-dimensional and razor-thin. This ignores potential dynamical consequences of vertical gas motions and related mixing, which was shown important in inducing non-steady gas motions across spiral shocks (e.g., Kim & Ostriker 2006; Kim et al. 2006, 2010). Second, we adopt an isothermal equation of state for the gas, corresponding to the warm phase, and do not consider radiative cooling and heating required for production and transitions of multiphase gas (e.g., Field 1965; Wolfire et al. 2003; McKee & Ostriker 2007). We also ignore the effects of outflows, winds, and radiative feedback from young stars, which may be of crucial importance in setting up the equilibrium pressure in galactic planes, thereby regulating star formation in disk galaxies (e.g., Ostriker et al. 2010; Ostriker & Shetty 2011; Shetty & Ostriker 2012). Finally, we in the present work do not consider the effects of spiral arms that may supply gas to the bar regions. With these caveats, the numerical models presented in this paper should be considered as a first step toward more realistic modeling of star formation in nuclear rings.

This paper is organized as follows. In Section 2, we describe the numerical methods and parameters used for our time-dependent simulations. In Section 3, we present the temporal evolution of SFRs, and their dependence on the model parameters. The age gradients of star clusters in the azimuthal and radial directions as well as properties of star clusters and dense clouds are discussed in Section 4. In Section 5, we summarize our main results and discuss their astronomical implications.

2. MODEL AND METHOD

To study star formation in nuclear rings of barred galaxies, we extend the numerical models studied in Paper I by including self-gravity, conversion of gas to stars, and feedback from star formation. In this section, we briefly summarize the current models and describe our handling of star formation and feedback. The reader is referred to Paper I for more detailed description of the numerical models.

2.1. *Galaxy Model*

We initially consider an infinitesimally-thin, rotating disk. The disk is assumed to be unmagnetized and isothermal with sound speed of $c_s = 10$ km s^{-1}. The external gravitational potential responsible for the disk rotation consists of four components: a stellar disk, a stellar bulge, a non-axisymmetric stellar bar, and a central BH with mass $M_{\rm BH} = 4\times10^7$ M$_\odot$. This gives rise to a rotation curve that is almost flat at $v_c \sim 200$ km s^{-1} in the bar region and its outside. The presence of the BH makes the rotation velocity rise as $v_c \propto (M_{\rm BH}/r)^{1/2}$ toward the galaxy center. The bar potential is modeled by a Ferrers (1887) prolate spheroid with semi-major and minor axes of 5 kpc and 2 kpc, respectively. The bar is rigidly rotating with a pattern speed $\Omega_b = 33$ km s^{-1} kpc^{-1}, which places the corotation resonance radius at $r = 6$ kpc and the inner Lindblad resonance (ILR) radius at $r = 2.2$ kpc. The corresponding orbital time is $t_{\rm orb} = 2\pi/\Omega = 186$ Myr. In our models, the bar potential is turned on over the bar growth time scale $\tau_{\rm bar}$, while the central density of the spheroidal component (bar plus bulge) is kept fixed. We vary $\tau_{\rm bar}$ to study situations where the bar grows at a different rate. The mass of the bar, when it is fully turned on, is set to 30% of the total mass of the spheroidal component within 10 kpc. All the models are run until 1 Gyr.

Table 1
Model Parameters

Model (1)	Σ_0(M$_\odot$ pc^{-2}) (2)	$\tau_{\rm bar}/t_{\rm orb}$ (3)	$f_{\rm mom}$ (4)
noSG	20	1	0.
U05	5	1	0.75
U10	10	1	0.75
U20	20	1	0.75
U30	30	1	0.75
M25	20	1	0.25
M50	20	1	0.50
FB05	20	0.5	0.75
FB20	20	2	0.75
FB40	20	4	0.75
E30	30	1	0.75
E50	50	1	0.75
E100	100	1	0.75

Note. — Gas surface density in Models with the prefix "E" initially have an exponential distribution $\Sigma = \Sigma_0 \exp{(-r/3.5 \text{ kpc})}$. All the other models have a uniform density distribution $\Sigma = \Sigma_0$.

As in Paper I, we integrate the basic equations of ideal hydrodynamics in a frame corotating with the bar. We use the CMHOG code in cylindrical polar coordinates (r, ϕ). CMHOG is third-order accurate in space and has very little numerical diffusion (Piner et al. 1995). To resolve the central region with high accuracy, we set up a logarithmically-spaced cylindrical grid over $r = 0.05$ kpc to 8 kpc. The number of zones in our models is 1024 in the radial direction and 632 in the azimuthal direction covering the half-plane from $\phi = -\pi/2$ to $\pi/2$. The corresponding spatial resolution is 0.25 pc, 5 pc, and 40 pc at the inner boundary, at $r = 1$ kpc where most star formation takes places, and at the outer radial boundary, respectively. We adopt the outflow and continuous boundary conditions at the inner and outer radial boundaries, respectively, while taking the periodic boundary conditions at $\phi = \pm\pi/2$.

Our models consider conversion of gas to stars, as will be explained in Section 2.2 in detail. Since the total gas mass transformed to stars is significant, it is important to evolve them under the combined gravitational potential of the gas and stars. At each time step, we calculate the stellar surface density on the grid points via the triangular-shaped-cloud assignment scheme (Hockney & Eastwood 1988) from the distribution of stellar particles. We then solve the Poisson equation to obtain the gravitational potential of the total (gas plus star) surface density, using the Kalnajs (1971) method presented in Shetty & Ostriker (2008).[1] To allow for dilution of gravity due to finite thickness H of the combined disk, we take $H/r = 0.1$ as a softening parameter in the potential calculation.

To explore the dependence of SFR upon the total gas content and the way the gas is spatially distributed, we initially consider gaseous disks with either uniform surface density Σ_0 or an exponential distribution $\Sigma_0 \exp(-r/R_d)$ with the scale length of $R_d = 3.5$ kpc. We also vary the fraction $f_{\rm mom}$ of the radial momentum from SNe imparted to the disk in the in-plane direction relative to what would be the total radial momentum in a three-dimensional uniform medium (see Section 2.2). We run a total of 13 models that differ in Σ_0, $\tau_{\rm bar}$, and $f_{\rm mom}$. Table 1 lists the model parameters. Column (1) lists each model. Models with the prefix "E" have an exponential disk, while all the others have a uniform disk. Model noSG is a control model that does not include self-gravity and star formation. Column (2) lists Σ_0 of the disk. Column (3) gives the bar growth time $\tau_{\rm bar}$ in units of $t_{\rm orb}$, while Column (4) gives $f_{\rm mom}$. We take Model U20 with $\Sigma_0 = 20$ M$_\odot$ pc^{-2}, $\tau_{\rm bar}/t_{\rm orb} = 1$, and $f_{\rm mom} = 0.75$ as our fiducial model. All the models initially have a Toomre Q parameter greater than unity, so that they are gravitationally stable in the absence of a bar potential. However, nuclear rings that form near the center achieve large density, enough to undergo runaway collapse to form stars.

2.2. *Star Formation and Feedback*

To model star formation and ensuing feedback, we first identify high-density regions whose average surface density $\langle\Sigma\rangle$ within a radius $R_{\rm SF}$ exceeds a critical density. The natural choice for the threshold density would be

$$\Sigma_{\rm th} = \frac{c_s^2}{2GR_{\rm SF}} = 1160\ {\rm M_\odot\ pc^{-2}} \left(\frac{c_s}{10\ {\rm km\ s^{-1}}}\right)^2 \left(\frac{R_{\rm SF}}{10\ {\rm pc}}\right)^{-1}, \tag{1}$$

from the Jeans condition. While it is desirable to choose a small value for the sizes of star-forming regions, we take $R_{\rm SF} = 10$ pc because of numerical resolution: a star-forming cloud at $r \sim 1$ kpc encloses typically ~ 13 grid points.

Not all clouds with $\langle\Sigma\rangle \geq \Sigma_{\rm th}$ immediately undergo gravitational collapse and star formation since we need to consider the star formation efficiency as well as the computational time step (Kim et al. 2011). The SFR expected from a cloud with mass $M_{\rm cloud} = \pi R_{\rm SF}^2 \langle\Sigma\rangle$, from the Schmidt (1959) law, is

$$\mathrm{SFR} = \epsilon_{\rm ff} \frac{M_{\rm cloud}}{t_{\rm ff}} \quad \text{for } \langle\Sigma\rangle \geq \Sigma_{\rm th}, \tag{2}$$

where $\epsilon_{\rm ff}$ is the star formation efficiency per free-fall time, $t_{\rm ff}$, defined by

$$t_{\rm ff} = \left(\frac{3\pi}{32G\langle\rho\rangle}\right)^{1/2} = 3.4\ {\rm Myr} \left(\frac{\langle\Sigma\rangle}{1160\ {\rm M_\odot\ pc^{-2}}}\right)^{-1/2}, \tag{3}$$

assuming a disk scale height of 100 pc. We take $\epsilon_{\rm ff} = 0.01$, consistent with theoretical and observational estimates (e.g., Krumholz & McKee 2005; Krumholz & Tan 2007).

The star formation probability of an eligible cloud with $\langle\Sigma\rangle \geq \Sigma_{\rm th}$ in a time interval Δt is then given by $p = 1 - \exp(-\epsilon_{\rm ff}\Delta t/t_{\rm ff}) \approx \epsilon_{\rm ff}\Delta t/t_{\rm ff}$ (e.g., Hopkins et al. 2011). For a given computational time step Δt, the probability p calculated in our models is typically $\sim 10^{-6} - 10^{-5}$, much smaller than unity. In each time step, we thus generate a uniform random number $\mathcal{N} \in [0, 1)$, and turn on star formation only if $\mathcal{N} < p$. When a cloud undergoes star formation, we create a particle with mass M_*, and convert 90% of the cloud mass to the particle mass. The initial position and velocity of the particle are set equal to the density-weighted mean values of the parent cloud within $R_{\rm SF}$. Each particle has a mass in the range $M_* \sim 10^5 - 10^7$ M$_\odot$, which is about $\sim 1 - 10^2$ times larger than the masses of observed clusters in nuclear rings (e.g., Maoz et al. 2001; Benedict et al. 2002; see also Portegies Zwart et al. 2010). Therefore, a massive single particle in our models can be regarded as representing an unresolved group of star clusters rather than an individual cluster.

We treat SN feedback using simple momentum input to the surrounding gaseous medium. We consider only Type II SN events since our models run only until 1 Gyr. Since we do not resolve individual stars in a cluster or their group, we assume that all SN explosions occur simultaneously. Stars with mass between 8 M$_\odot$ and 40 M$_\odot$ explode as Type II SNe (Heger et al. 2003), which comprise about 7% of the cluster mass under the Kroupa (2001) initial mass function. The mean mass of SN progenitors is then ~ 14 M$_\odot$, indicating that the number of SNe exploding from a cluster (or their group) with mass M_* is $\mathcal{N}_{\rm SN} = M_*/(200\ {\rm M_\odot})$, with the total ejected mass $M_{\rm ejecta} = 0.07 M_*$ returning back to the ISM. Between star formation and SN explosions, we allow a time delay of 10 Myr, corresponding to the mean life time of Type II SN progenitors (e.g., Lejeune & Schaerer 2001). Note that the orbital time of gas in nuclear rings is typically ~ 25 Myr in our models, so that star clusters move by about 150° in the azimuthal angle from the formation sites before experiencing SN explosions.

Each feedback, corresponding to $\mathcal{N}_{\rm SN}$ simultaneous SNe, injects mass and radial momentum in the form of an expanding shell. In the momentum-conserving stage, a single SN with energy 10^{51} erg would drive radial momentum $P_{\rm rad,3D} = 3 \times 10^5 \epsilon_0^{7/8} (\Sigma/1\ {\rm M_\odot\ pc^{-2}})^{-1/4}$ M$_\odot$ km s^{-1} to the surrounding gas if the background medium is uniform and in three dimensions, where ϵ_0 is the SN energy in units of 10^{51} erg (e.g., Chevalier 1974; Shull 1980; Cioffi et al. 1988). The dependence of $P_{\rm rad,3D}$ on Σ is due to the fact that the shell expansion in the Sedov phase is slow when the background surface density is large. Since our model disks are razor-thin by ignoring the vertical direction, the momentum imparted to the gas in the simulation domain would be smaller than $P_{\rm rad,3D}$. Let $f_{\rm mom}$ denote the fraction of the total radial momentum that goes into the in-plane direction. If the expansion is isotropic, $f_{\rm mom} \sim 75\%$ (Kim et al. 2011), but $f_{\rm mom}$ can be smaller in a vertically stratified disk since it is easier for a shell to expand along the vertical direction. The total momentum of a shell from each feedback is thus set to

---

[1] We ignore the gravity from the initial gas distribution in order to make the initial rotation curve the same with that in the non-self-gravitating counterpart.

$$P_{\rm sh} = 3\times 10^5 f_{\rm mom}\, \mathcal{N}_{\rm SN}^{7/8} \left(\frac{\Sigma}{1\ {\rm M_\odot\ pc^{-2}}}\right)^{-1/4}\ {\rm M_\odot\ km\ s^{-1}}. \tag{4}$$

In this paper, we take $f_{\rm mom} = 0.75$ as a standard value, but run some models with lower $f_{\rm mom}$ to study the effect of $f_{\rm mom}$ on the SFR (see Table 1).

As the initial radius of a shell, we take $R_{\rm sh} = 40$ pc, corresponding to the shell size at the end of the Sedov phase when $\mathcal{N}_{\rm SN} = 10^3$ and the background density is $\Sigma = 10^3\ {\rm M_\odot\ pc^{-2}}$, the typical mean density of nuclear rings when star formation is active. When feedback occurs from a particle, we redistribute the mass and momentum within a circular region with radius $R_{\rm sh}$ centered at the particle by taking their spatial averages. We then add the shell momentum density

$$\Sigma \mathbf{v}_{\rm sh} = \begin{cases} P_{\rm max}\left(\frac{R}{R_{\rm sh}^2}\right)\mathbf{R}, & r \le R_{\rm sh}, \\ 0, & r > R_{\rm sh}, \end{cases} \tag{5}$$

to the gas momentum density in the in-plane direction, and $M_{\rm ejecta}/(\pi R_{\rm sh}^2)$ to the gas surface density, while reducing the particle mass by $M_{\rm ejecta}$. In equation (5), $\mathbf{R}$ denotes the position vector relative to the particle location and $P_{\rm max} = 2P_{\rm sh}/(\pi R_{\rm sh}^2)$ is the momentum per unit area at $r = R_{\rm sh}$. Note that $v_{\rm sh}(R) \propto R^2$ ensures an initially divergence-free condition at the feedback center (e.g., Kim et al. 2011).

3. STAR FORMATION IN NUCLEAR RINGS

In this section, we first describe overall evolution of our numerical simulations. We then present the temporal variations of SFRs and their dependence on the gas mass, the bar growth time, and $f_{\rm mom}$, as well as the relationship between the SFR surface density and the gas surface density. The properties of star clusters and gas clouds in the rings are analyzed in the next section.

3.1. *Overall Gas Evolution*

We begin by presenting evolution of our standard model U20 that has a uniform density $\Sigma_0 = 20\ {\rm M_\odot\ pc^{-2}}$ initially. Evolution of the other models is qualitatively similar, although more massive disks show more active star formation. In all models, star formation occurs mostly in the nuclear rings.[2] Figure 1 plots snapshots of the gas distributions as well as the positions of star clusters in Model U20 at a few selected epochs. The left panels show the gas density in logarithmic scales in the 5 kpc regions, with the solid ovals indicating the outermost x_1-orbit that cuts the x- and y-axes at $x_c = 3.6$ kpc and $y_c = 4.7$ kpc, respectively. The middle and right panels zoom in the central 2 kpc regions. In the right panels, small dots indicate star clusters older than 10 Myr, while asterisks correspond to young clusters with age < 10 Myr: the upper right colorbar represents their ages. In all panels, the bar is oriented vertically along the y-axis and remains stationary. The gas inside the corotation resonance is rotating in the counterclockwise direction.

Early evolution of Model U20 before $t = 0.1$ Gyr is not much different from non-self-gravitating models presented in Kim et al. (2012a). The imposed non-axisymmetric bar potential perturbs gas orbits to create overdense ridges at the far downstream side from the bar major axis. Only the region inside the outermost x_1-orbit responds strongly to the bar potential. Before the bar is fully turned on (i.e., $t < \tau_{\rm bar}$), no closed x_1- and x_2-orbits exist since the external gravitational potential varies with time. During this time, the gas streamlines are highly transient as they try to adjust to the time-varying potential. The overdense ridges grow with time and move slowly toward the bar major axis, developing into dust-lane shocks. The gas passing through the shocks loses angular momentum and flows radially inward along the dust lanes. The radial velocity of the inflowing gas is so large that it is not halted at the ILR (Paper I). It gradually rotates faster due to the Coriolis force, and eventually forms a nuclear ring after hitting the dust lane at the opposite side. Produced by supersonic collisions of two gas streams, the contact points between the ring and the dust lanes have the largest density in the ring, and can thus be preferred sites of star formation.

Over time, the nuclear ring shrinks in size and the contact points rotate in the azimuthal direction.[3] To illustrate this more clearly, Figure 2 plots the temporal and radial variations of the azimuthally averaged surface density in the central regions of Model U20 and its non-self-gravitating counterpart, Model noSG. The horizontal dashed line marks the location of the ILR. The ring is beginning to form at $t \sim 0.1$ Gyr at the galactocentric radius of $r \sim 1$ kpc, well inside the ILR. At early time when the bar is growing, the ring is not in an equilibrium position and its shape is quite different from x_2-orbits: the major axis of the ring is inclined to the x-axis by -30° at $t = 0.15$ Gyr (Fig. 1a). As the ring material continuously interacts with the bar potential, the contact points rotate in the counterclockwise direction. At $t \sim 0.2$ Gyr, the ring settles on one of the x_2-orbits, and the contact points are located close the bar minor axis.

At the same time, the ring becomes smaller in size due to the addition of low-angular momentum gas from outside as well as by collisions of the ring material whose orbits are perturbed by thermal pressure (Paper I). When self-gravity is absent, the decreasing rate of the ring radius is $d\ln r_{\rm NR}/dt \sim -1.5\ {\rm Gyr^{-1}}$ until $t \lesssim 0.8$ Gyr. After this time, the ring is so small that strong centrifugal force inhibits further decay of the ring. In Model U20 with self-gravity included, on the other hand, strong self-gravitational potential of the ring makes the gas or-

---

[2] In Model U30, the bar-end regions, often called ansae, form stars as well, although the associated SFR is less than 3% compared to the ring star formation.

[3] As pointed out by the referee, Figure 1 shows that the ring starts out fairly elongated and titled relative to the bar and becomes rounder with time. Note that the shape of the ring in Model U20 at $t = 0.15$ Gyr is remarkably similar to that of a highly-elongated nuclear ring in ESO 565-11 observed by Buta et al. (1999), although the latter is $\sim$ 2–3 times bigger than the former.

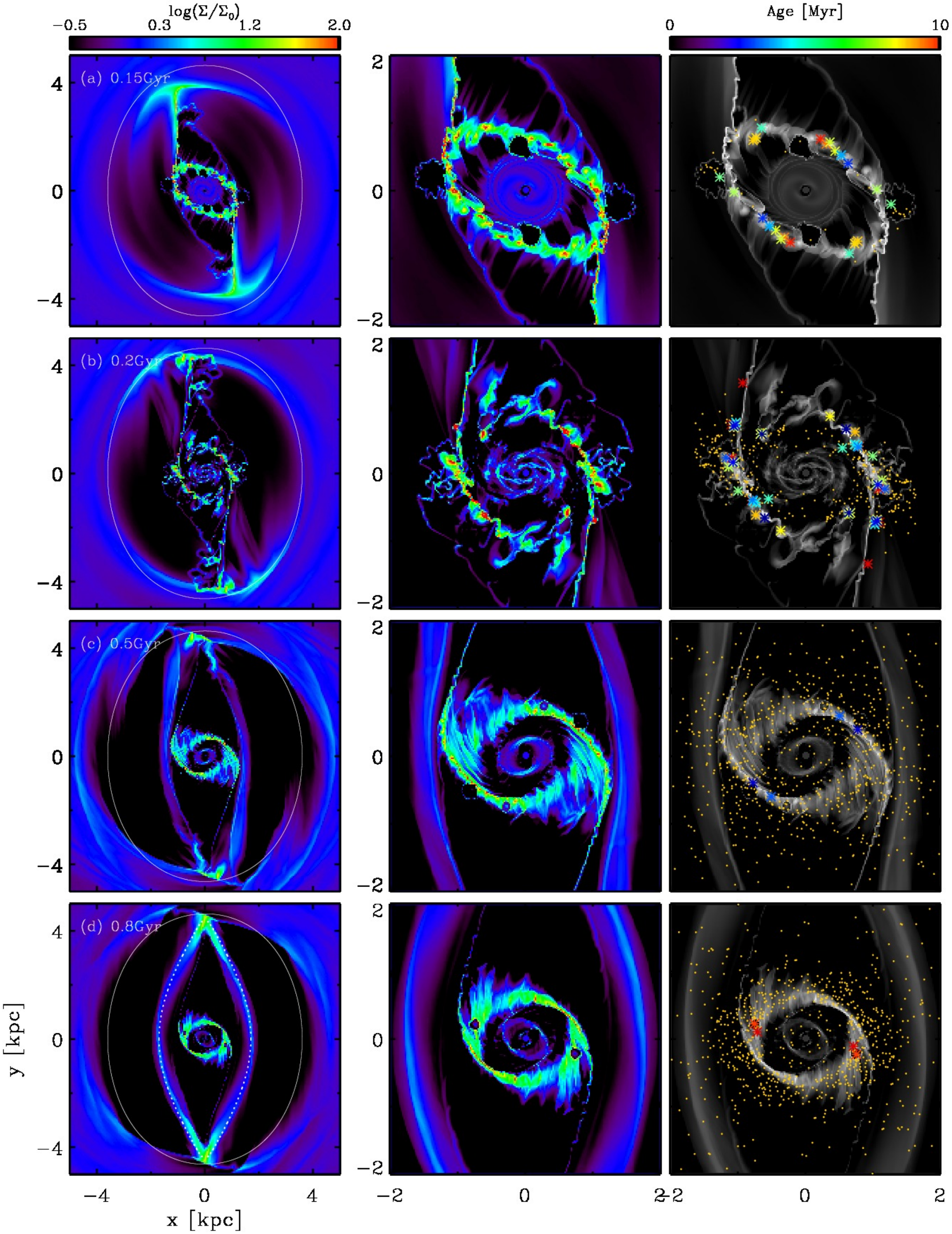

Figure 1. Snapshots of logarithm of gas density (color scale) as well as the locations of star clusters in Model U20 at $t = 0.15, 0.2, 0.5, 0.8$ Gyr. The left panels show the 5 kpc regions, while the middle and right panels zoom in the central 2 kpc regions. The upper left colorbar labels $\log(\Sigma/\Sigma_0)$. The solid ovals in the left panels draw the outermost x_1-orbit that cuts the x- and y−axes at $x_c = 3.6$ kpc and $y_c = 4.7$ kpc. The dotted curve in (d) is an x_1-orbit with $x_c = 1.7$ kpc and $y_c = 4.4$ kpc that traces the inner ring. Small dots in the right panels denote clusters older than 10 Myr, while asterisks represent clusters younger than 10 Myr, with the upper right colorbar displaying their ages.

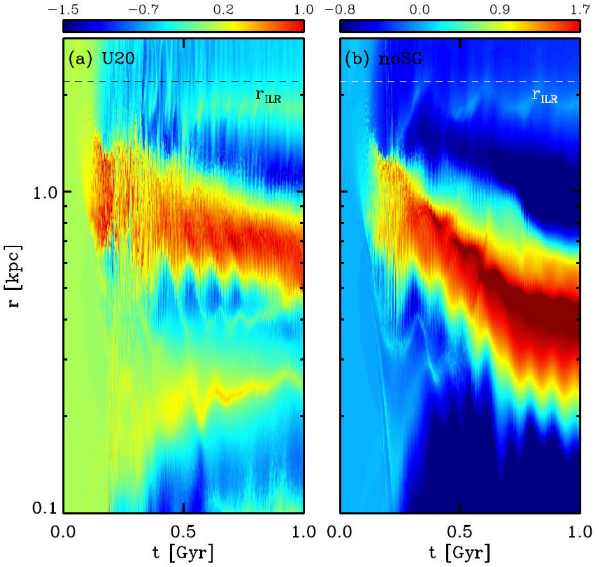

Figure 2. Temporal and radial variations of the azimuthally averaged surface density in logarithmic scale for (a) Model U20 and (b) Model noSG. The horizontal dashed line in each panel marks the location of the inner Lindblad resonance. The colorbars label $\log(\Sigma/\Sigma_0)$. The decreasing rate of the ring size is smaller when self-gravity and star formation are included.

bits relatively intact, reducing the ring decay rate to $d\ln r_{\rm NR}/dt \sim -0.4$ Gyr^{-1}. The decrease of the ring size in turn causes the contact points to move radially inward and rotate further in the counterclockwise direction (but not more than $\sim 30°$).

As Figure 1 shows, the bar region (i.e., inside the outermost-x_1 orbit) becomes evacuated quite rapidly. This is because the bar potential is efficient in removing angular momentum from the gas only in the bar region, while its influence on the gas orbits outside the outermost-x_1 orbit is not significant. By $t \sim 0.3$ Gyr, most of the gas in the bar region is transferred to the ring. The amount of the gas added to the bar region from outside is much smaller than that lost to the ring, which causes the mass inflow rate to the ring to decrease dramatically with time (see Section 3.2).

Figure 1d shows that at late time there is a substantial amount of gas trapped in around an x_1-orbit with $x_c = 1.7$ kpc and $y_c = 4.4$ kpc, shown as a dotted line. This elongated gaseous structure circumscribing the dust lanes and nuclear ring is called the inner ring (e.g., Buta 1986; Regan et al. 2002): we term the corresponding x_1-orbit the inner-ring x_1-orbits. The formation of the inner ring in our model is as follows. As mentioned before, the dust-lane shocks form first at far downstream and moves toward the bar major axis as the bar potential grows. During this time, much of the gas in the bar region infalls to the nuclear region. Near the time when the bar attains its full strength, the dust lanes find their equilibrium positions on an x_1-orbit, still at the leading side from the bar major axis. The inner ring starts to form at this time, by gathering the residual material located between the outermost and inner-ring x_1-orbits. Some gases located outside the outermost x_1-orbit experience collisions near the bar ends where x_1-orbits crowd, and are then able to lower their orbits to the inner-ring x_1-orbit, increasing the inner-ring mass. In Model U20, the gas added to the inner ring from outside of the outermost x_1-orbit is about 70% of the total inner-ring mass at $t = 1$ Gyr. Most of the gas inside the inner-ring x_1-orbit had already transited to the nuclear ring by experiencing the dust-lane shocks before the bar was fully turned on.

3.2. *Star Formation Rate*

Figure 3 plots the time evolution of the SFR, the mass inflow rate to the nuclear ring $\dot{M}_{\rm NR} \equiv \int_0^{2\pi} \Sigma v_r r d\phi$ (measured at $r = 1.5$ kpc), and the total gas mass inside the nuclear ring $M_{\rm NR}$ in Model U20. Here v_r denotes the radial velocity of the gas. In plotting these profiles, we take a boxcar average, with a window of 20 Myr. In this model, the bar potential grows over the time scale of $\tau_{\rm bar} = 0.19$ Gyr, and the first star formation takes place at the contact points at $t = 0.12$ Gyr. As the bar grows further, the dust-lane shocks become stronger, increasing the amount of the infalling gas to the ring. $\dot{M}_{\rm NR}$ attains a peak value ~ 8 M$_\odot$ yr^{-1} at $t = 0.15$ Gyr, which coincides with the time of highest density of the dust lanes (see Fig. 5 of Paper I). The decay of $\dot{M}_{\rm NR}$ after the peak is caused by the fact that only the gas inside the outermost x_1-orbit responds strongly to the bar potential, while the outer region is not much affected. Similarly, the SFR exhibits a strong burst with a maximum value ~ 8 M$_\odot$ yr^{-1}, which occurs ~ 30 Myr after the peak of $\dot{M}_{\rm NR}$. The associated SN feedback produces many holes in the gas distribution, driving a huge amount of kinetic energy to the surrounding medium. Note that the nuclear ring, albeit somewhat patchy, is overall well maintained despite energetic momentum injections (Fig. 1b).

When the mass inflow rate to the ring is very large, star formation occurring at the contact points alone is unable to consume the whole inflowing gas. As we will show in Section 4.1, the maximum gas consumption rate afforded to the contact points is estimated to be about 1 M$_\odot$ yr^{-1} for the parameters we adopt. Any surplus inflowing gas passes by the contact points and is subsequently added to the ring that is clumpy. Some overdense regions in the ring are soon able to achieve the mean density larger than the critical value and undergo star formation, increasing the SFR rapidly. Since the star-forming regions are randomly distributed in the ring, there is no obvious azimuthal age gradient of star clusters in this high-SFR phase.

Particles spawned from star formation orbit about the galaxy center under the total gravity, but they do not feel gas pressure that is quite strong in the nuclear ring. In addition, the gaseous ring becomes smaller in size with time. Thus, the orbits of star particles increasingly deviate from the gaseous orbits over time. When stars in clusters explode as SNe, they are not always located in the ring. A majority of star clusters are still in the ring, while there are some clusters ($\sim 10\%$) located exterior to the ring. SNe occurring in the ring have relatively small radial velocities due to a large background density, and the shell expansion is limited by the surrounding dense gas. On the other hand, SNe exploding outside the ring can have very large expansion velocities enough to send the neighboring gas out to the bar-end regions. The expelled gas sweeps up the gas on its way to the bar-end regions, passes through the dust-lane shocks again, and falls back radially inward along the dust lane. This in-

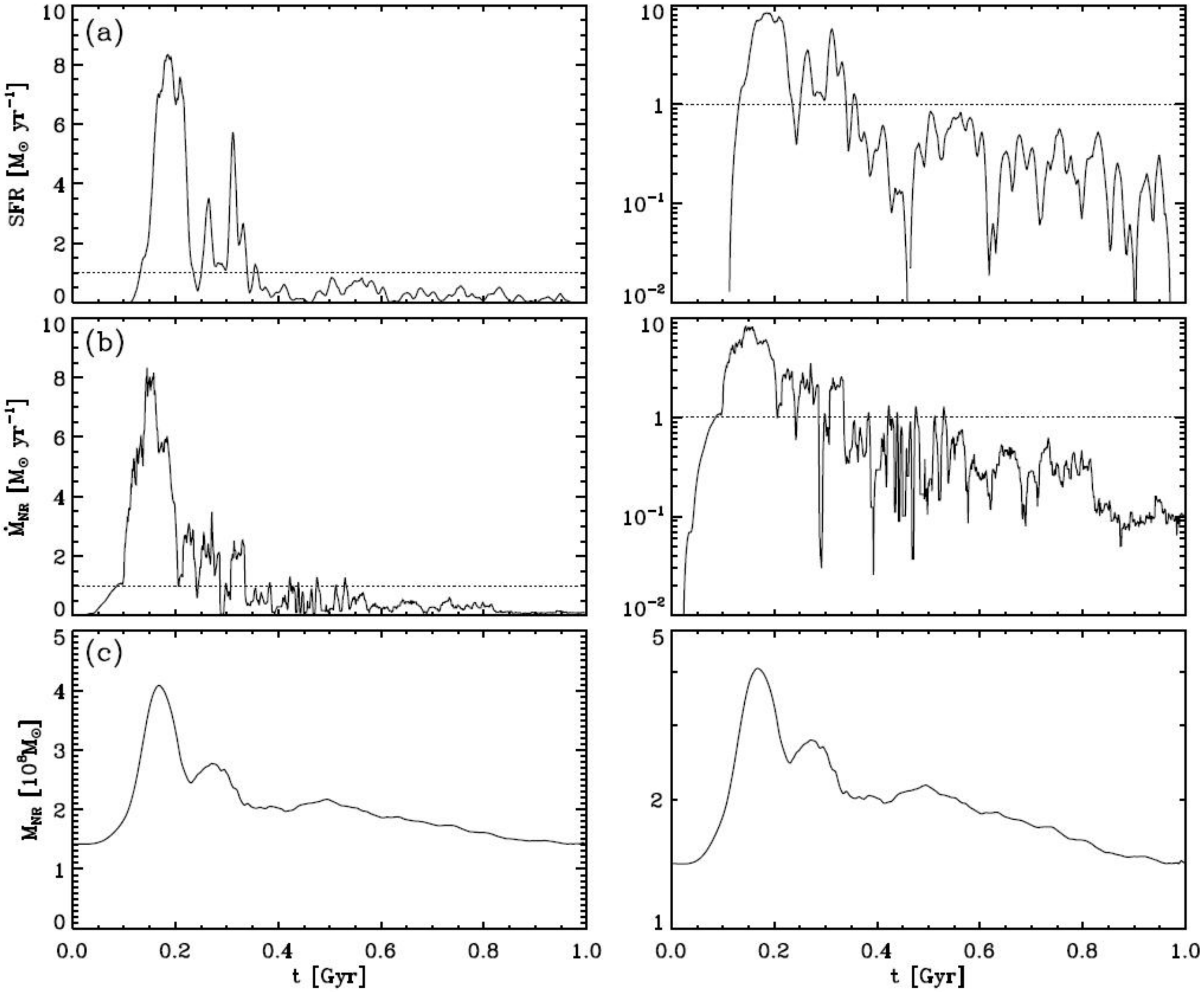

Figure 3. Temporal variations of (a) the SFR, (b) the mass inflow rate $\dot{M}_{\rm NR}$ to the nuclear ring, and (c) the total gas mass $M_{\rm NR}$ in the nuclear ring of Model U20. The ordinate is in linear scale in the left panels, while it is in logarithmic scale in the right panels. In (a) and (b), the horizontal dotted lines indicate the reference rate of 1 M$_\odot$ yr^{-1}.

creases $\dot{M}_{\rm NR}$ temporarily during $t = 0.2$–0.35 Gyr, with the associated short bursts of star formation at $t = 0.27$ and 0.32 Gyr in Model U20.

At $t = 0.3$ Gyr, the bar region is almost emptied, except for the inner ring, as most of the gas is already lost to the ring. Other than intermittent infalls of the expelled and swept-up gas from SNe, the mass inflow rate from the inner ring to the nuclear ring and the related SFR become fairly small. In addition, $M_{\rm NR}$ is reduced to below 2×10^8 M$_\odot$ in Model U20 since star formation consumes the gas in the ring, which also decreases the SFR (Fig. 3). As most of the gas in the bar region inside the outermost x_1-orbit is almost lost to star formation, the galaxy evolves into a quasi-steady state where star formation is limited to small regions near the contact points (Fig. 1d).

3.3. *Parametric Dependence of SFR*

Figure 4 compares the SFRs from (left) uniform-disk and (right) exponential-disk models with different Σ_0. In all models, the SFR displays a primary burst followed by a few secondary bursts, with time intervals of $\sim 50 - 80$ Myr, before becoming reduced to below 1 M$_\odot$ yr^{-1}. The primary burst is associated with the rapid gas infall due to angular momentum loss at the dust-lane shocks, while the secondary bursts are caused by the re-infall of the ejected gas via SN feedback out to the bar region. Models with larger Σ_0 start to form stars earlier and have a larger value of the maximum star formation rate, SFR$_{\rm max}$. The duration of active star formation, $\Delta t_{\rm SF}$, defined by the time span when SFR $\geq$ SFR$_{\rm max}/2$, is also larger for models with larger Σ_0, since the gas available for star formation is correspondingly larger. Models U20 and E50 initially have a similar gas mass inside the outermost x_1-orbit, but Model E50 has larger SFR$_{\rm max}$ since the gas is more centrally concentrated and thus infalls more readily to the nuclear ring. Columns (2) and (3) of Table 2 list SFR$_{\rm max}$ and $\Delta t_{\rm SF}$ for all models. The phase of active star formation lasts only for $\sim 0.5\tau_{\rm bar}$ in all models.

Figure 5 shows how (left) the bar growth time and (right) the amount of the momentum injection affect the temporal behavior of the SFR. In models where the bar grows more rapidly, dust-lane shocks form earlier and

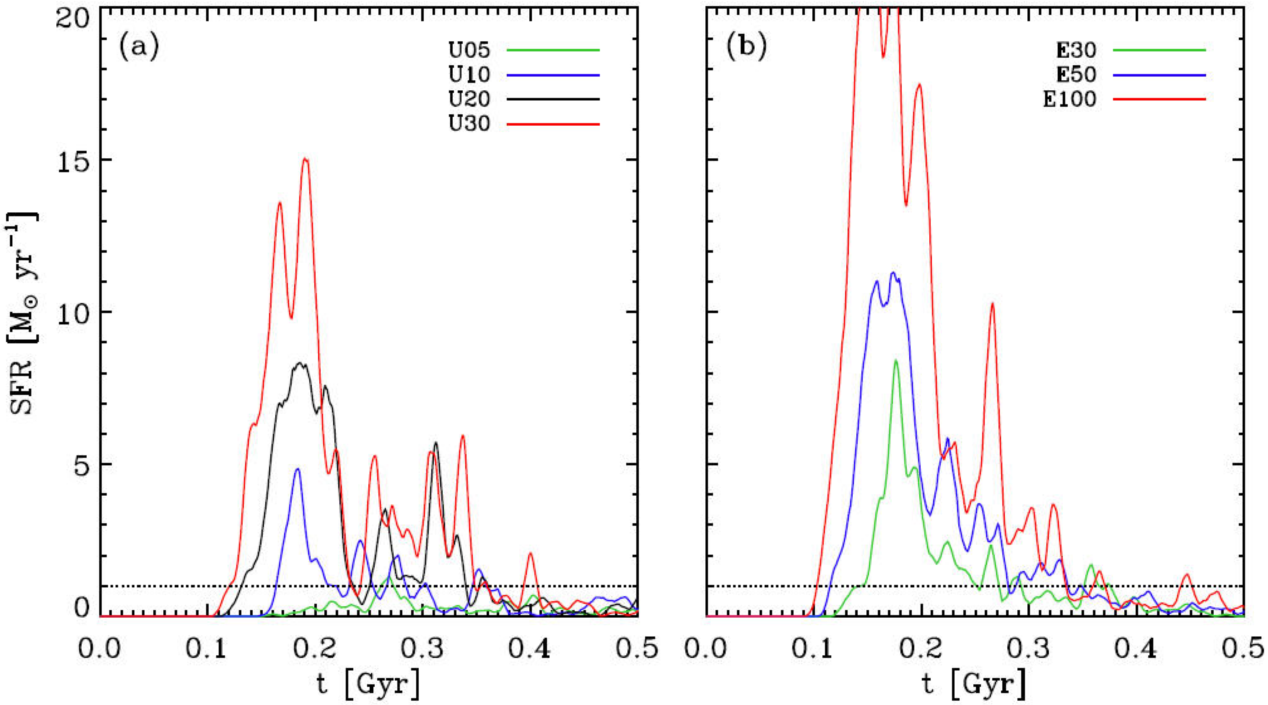

Figure 4. Temporal variations, over $t = 0 - 0.5$ Gyr, of the SFR for (a) the uniform-disk models and (b) the exponential-disk models with differing Σ_0. The horizontal dotted lines indicate SFR $= 1$ M$_\odot$ yr^{-1}. Models with larger gas mass inside the outermost x_1-orbit form stars earlier and at a larger rate.

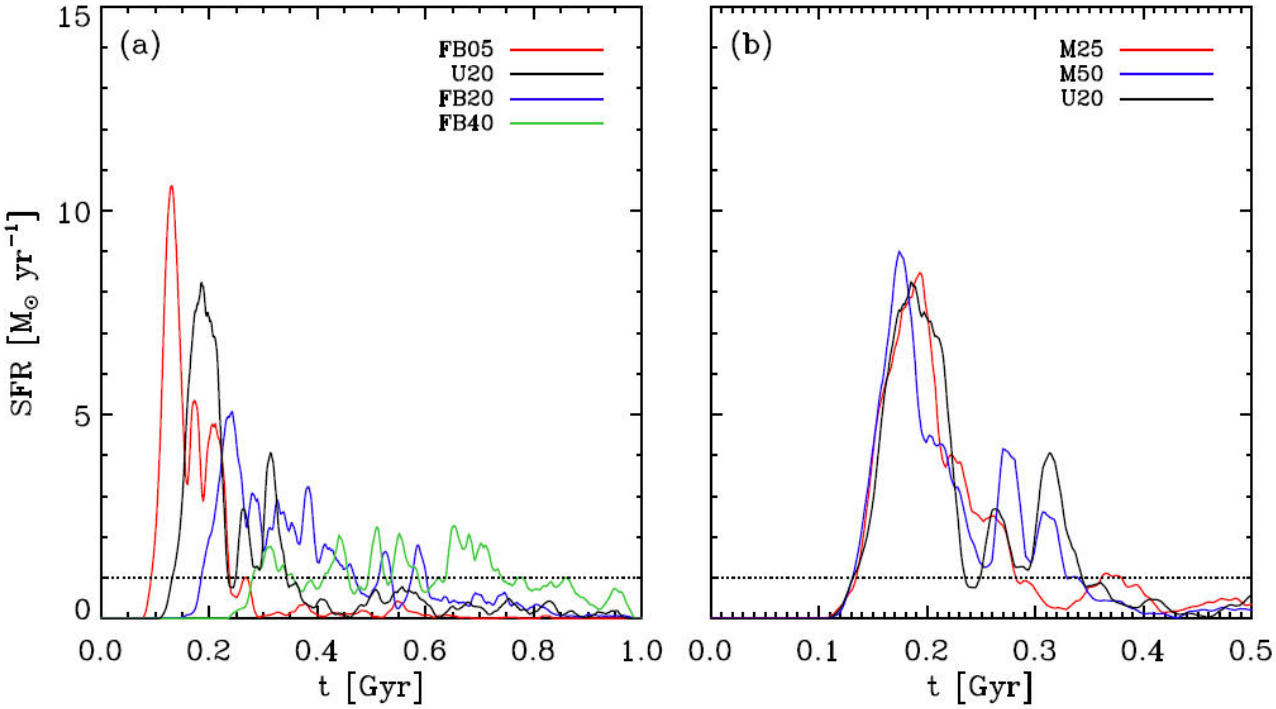

Figure 5. Temporal variations of the SFR for (a) models with differing the bar growth time $\tau_{\rm bar}$ and (b) models with different momentum injection $f_{\rm mom}$. Note that the range of the abscissa is 1 Gyr in (a) and 0.5 Gyr in (b). The horizontal dotted lines indicate SFR $= 1$ M$_\odot$ yr^{-1}.

Table 2
Simulation Outcomes

Model (1)	$\mathrm{SFR}_{\mathrm{max}}$ ($\mathrm{M}_\odot$ yr^{-1}) (2)	Δt_{SF} (Myr) (3)	M_*^{tot} ($10^8\mathrm{M}_\odot$) (4)	M_{x_1} ($10^8\mathrm{M}_\odot$) (5)	M_{NR} ($10^8\mathrm{M}_\odot$) (6)	β (7)	Γ (8)
noSG	-	-	-	10.66	8.03	-	-
U05	0.53	-	1.4	2.62	0.87	13.7	3.1
U10	3.55	42	3.3	5.33	1.39	14.4	2.6
U20	7.46	83	9.0	10.66	1.42	12.5	2.2
U30	11.8	83	13.3	15.99	2.36	12.6	2.2
M25	7.77	87	8.2	10.66	1.08	9.6	2.3
M50	7.78	77	8.7	10.66	1.55	10.8	2.2
FB05	9.83	68	8.9	10.66	1.62	12.3	2.2
FB20	4.04	163	8.7	10.66	1.73	9.7	2.2
FB40	1.94	392	7.2	10.66	2.75	7.4	3.0
E30	5.10	74	6.1	7.55	1.55	12.4	2.2
E50	10.4	77	10.1	12.59	1.41	6.3	2.2
E100	21.9	84	23.0	25.18	1.78	6.3	2.0

Note. — $\mathrm{SFR}_{\mathrm{max}}$ and Δt_{SF} denote the peak rate and the duration of active star formation with $\mathrm{SFR} \geq \mathrm{SFR}_{\mathrm{max}}/2$, respectively; M_*^{tot} is the total mass in stars at $t = 1$ Gyr; M_{x_1} is the total gas mass inside the outermost x_1-orbit at $t = 0$; M_{NR} is the mass of the nuclear ring at $t = 1$ Gyr; $\beta = d\log(t/\mathrm{yr})/d(r/\mathrm{kpc})$ is the radial age gradient of clusters; $\Gamma = -d\log N/d\log M_*$ is the power-law slope of the cluster mass functions.

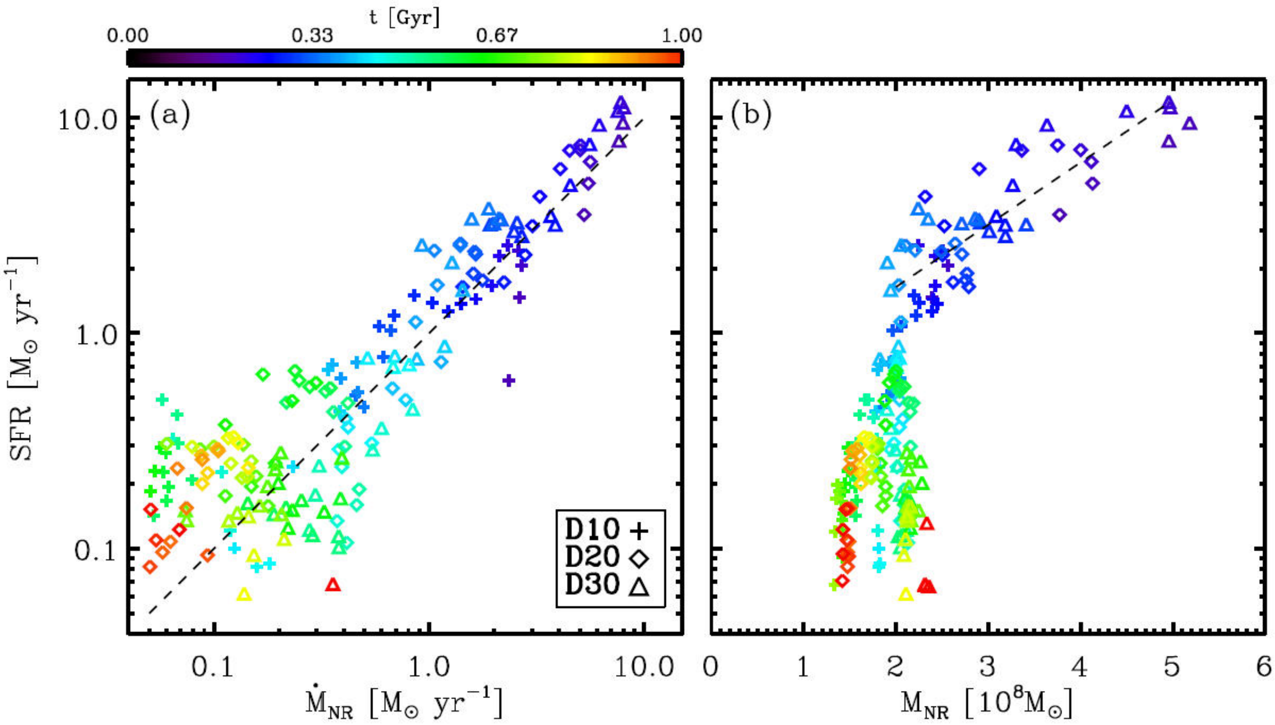

Figure 6. Dependence of the SFR on (a) the mass inflow rate $\dot{M}_{\mathrm{NR}}$ to the ring and (b) the total mass M_{NR} in the ring. The dashed line draws $\mathrm{SFR} = \dot{M}_{\mathrm{NR}}$ in (a), and $\mathrm{SFR} \propto \dot{M}_{\mathrm{NR}}^{0.3}$ in (b). The SFR is almost equal to $\dot{M}_{\mathrm{NR}}$ for the whole range of the SFR, while it is not well correlated with M_{NR} when $\mathrm{SFR} \leq 1$ $\mathrm{M}_\odot$ yr^{-1}.

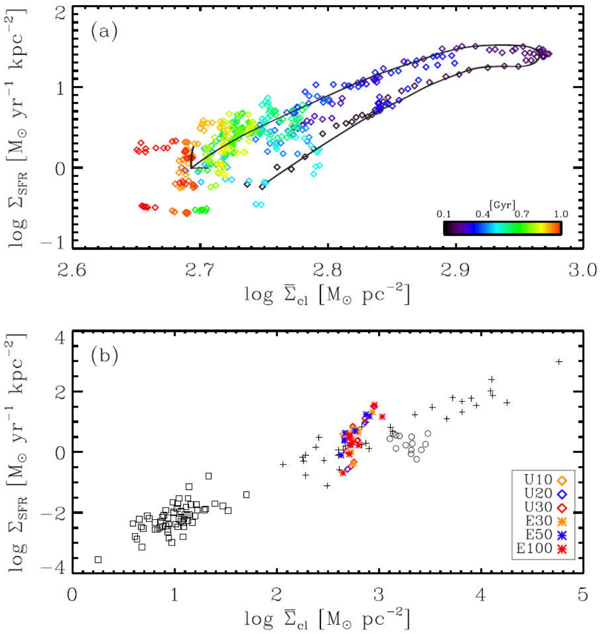

Figure 7. (a) Dependence of the SFR surface density $\Sigma_{\rm SFR}$ on the mean surface density $\bar{\Sigma}_{\rm cl}$ of dense clouds for Model U20. The colorbar indicates the epoch of star formation for each symbol, and the curved arrow denotes the mean evolutionary track in the $\Sigma_{\rm SFR} - \bar{\Sigma}_{\rm cl}$ plane. (b) $\Sigma_{\rm SFR} - \bar{\Sigma}_{\rm cl}$ relationship from our models compared to the observed Kennicutt-Schmidt law. Squares and pluses represent normal and circumnuclear starburst galaxies adopted from Kennicutt (1998), respectively, while circles are for spatially-resolved star-forming regions in NGC 1097 from Hsieh et al. (2011).

initiate stronger gas inflows. This causes star formation in models with smaller $\tau_{\rm bar}$ to occur at a higher rate and for a shorter period of time (see Table 2). The peak SFR is attained approximately at $t \sim (0.8-1)\tau_{\rm bar}$. This suggests that galaxies in which the bar forms more slowly are likely to have star formation less active instantaneously but extended for a longer period of time. Figure 5b shows that the SFR computed in our models is largely insensitive to $f_{\rm mom}$, although smaller $f_{\rm mom}$ makes the secondary bursts less active.

To directly address what controls star formation in nuclear rings, we plot in Figure 6 the dependence of the SFR (left) on the mass inflow rate to the ring and (right) on the gas mass in the ring for Models U10, U20, and U30. Color indicates the star formation epoch of each symbol. Even though there are large scatters especially when the SFR is low, the SFR is almost equal to $\dot{M}_{\rm NR}$ over two orders of magnitude variations in $\dot{M}_{\rm NR}$. The scatters in the SFR $-$ $\dot{M}_{\rm NR}$ relation are due to the fact that star formation is stochastic in our models and that it takes the gas some finite time ($\sim 10-30$ Myr) to travel from $r = 1.5$ kpc (where $\dot{M}_{\rm NR}$ is measured) to the nuclear ring. On the other hand, the SFR does not show a good correlation with $M_{\rm NR}$. While SFR $\propto M_{\rm NR}^{0.3}$ for SFR $\gtrsim 1$ M$_\odot$ yr^{-1}, it is almost independent of $M_{\rm NR}$ for SFR $\lesssim 1$ M$_\odot$ yr^{-1}. Note that the change in $M_{\rm NR}$ is less than a factor of 5 in Figure 6b, while the SFR varies by more than two orders of magnitude. This suggests that it is the mass inflow rate to the ring, rather than the ring mass, that determines the SFR in the nuclear ring. Conversely, the SFR can be a good measure of the mass inflow rate driven by the bar potential.

Column (4) of Table 2 gives the total mass in stars $M_*^{\rm tot}$ formed until the end of the run for each model. Columns (5) and (6) list the total gas mass M_{x_1} inside the outermost x_1-orbit in the initial disk and the mass of the nuclear ring $M_{\rm NR}$ at $t = 1$ Gyr, respectively. Note that M_{x_1} is approximately the maximum gas mass available for star formation in the ring. We find that the relation $M_*^{\rm tot} = M_{x_1} - M_{\rm NR}$, with $M_{\rm NR} = 2\times 10^8$ M$_\odot$ fixed, explains the numerical results fairly well, indicating that most of the gas inside the outermost x_1-orbit flows inward to form stars, with some residual gas remaining in the nuclear ring. Compared to Model U20 with $\tau_{\rm bar}/t_{\rm orb} = 1$, Model FB40 with $\tau_{\rm bar}/t_{\rm orb} = 4$ has $M_*^{\rm tot}$ about 20% smaller, since the gas in the bar region is still flowing in to the nuclear ring at the end of the run.

As will be discussed in more detail in Section 5.2, the overall temporal trend of the SFR (that is, rapid decline after a primary burst except for a few secondary bursts) found in our numerical models is largely similar to the numerical results of previous studies (e.g., Heller & Shlosman 1994; Knapen et al. 1995; Friedli & Benz 1995), but appears inconsistent with observations of Allard et al. (2006) and Sarzi et al. (2007) who found that star-forming nuclear rings live long, with multiple episodes of starburst activities. Since the ring SFR is controlled by the mass inflows rate to the rings, this implies that rings in real galaxies should be continually supplied with fresh gas from outside for quite a long period of time. Candidate mechanisms for additional gas inflows, over a time scale much longer than the bar growth time, include spiral arms and cosmic gas infalls, which are not included in this paper.

3.4. *Star Formation Law*

To explore the dependence of the local SFR on the local gas surface density, we define clouds as regions in the simulation domain whose density is larger than 300 M$_\odot$ pc^{-2}. This density roughly corresponds to the mean density of boundaries of gravitationally bound clouds in our models (see Section 4.4). While this choice of the minimum density for clouds is somewhat arbitrary, these clouds may represent giant molecular clouds and their complexes including hydrogen envelopes (e.g., Williams et al. 2000; McKee & Ostriker 2007).

At each time, we calculate the mean surface density $\bar{\Sigma}_{\rm cl}$ of, and the total area $A_{\rm cl}$ occupied by, the clouds distributed along the ring. The mean SFR surface density is then given by $\Sigma_{\rm SFR} = {\rm SFR}/A_{\rm cl}$. Figure 7a plots the resulting $\Sigma_{\rm SFR}$ as a function of $\bar{\Sigma}_{\rm cl}$ for Model U20. Color represents the time when each point is measured, while the curved arrow indicates the mean evolutionary direction in the $\Sigma_{\rm SFR}$–$\bar{\Sigma}_{\rm cl}$ plane. When the first star formation takes place ($t = 0.12$ Gyr), the ring has $\bar{\Sigma}_{\rm cl} \sim 560$ M$_\odot$ pc^{-2} and $\Sigma_{\rm SFR} \sim 0.5$ M$_\odot$ yr^{-1} kpc^{-2}. The radial gas inflow along the dust lanes increases $\Sigma_{\rm SFR}$ rapidly until it achieves a peak value at $t = 0.18$ Gyr. The corresponding increase of $\bar{\Sigma}_{\rm cl}$ is smaller since star formation reduces the gas content in the ring. After the peak, $\Sigma_{\rm SFR}$ decreases with decreasing $\dot{M}_{\rm NR}$, but it has a larger value, by a factor of $\sim 2-4$ on average, than that at the same $\bar{\Sigma}_{\rm cl}$ before the peak. This is because active

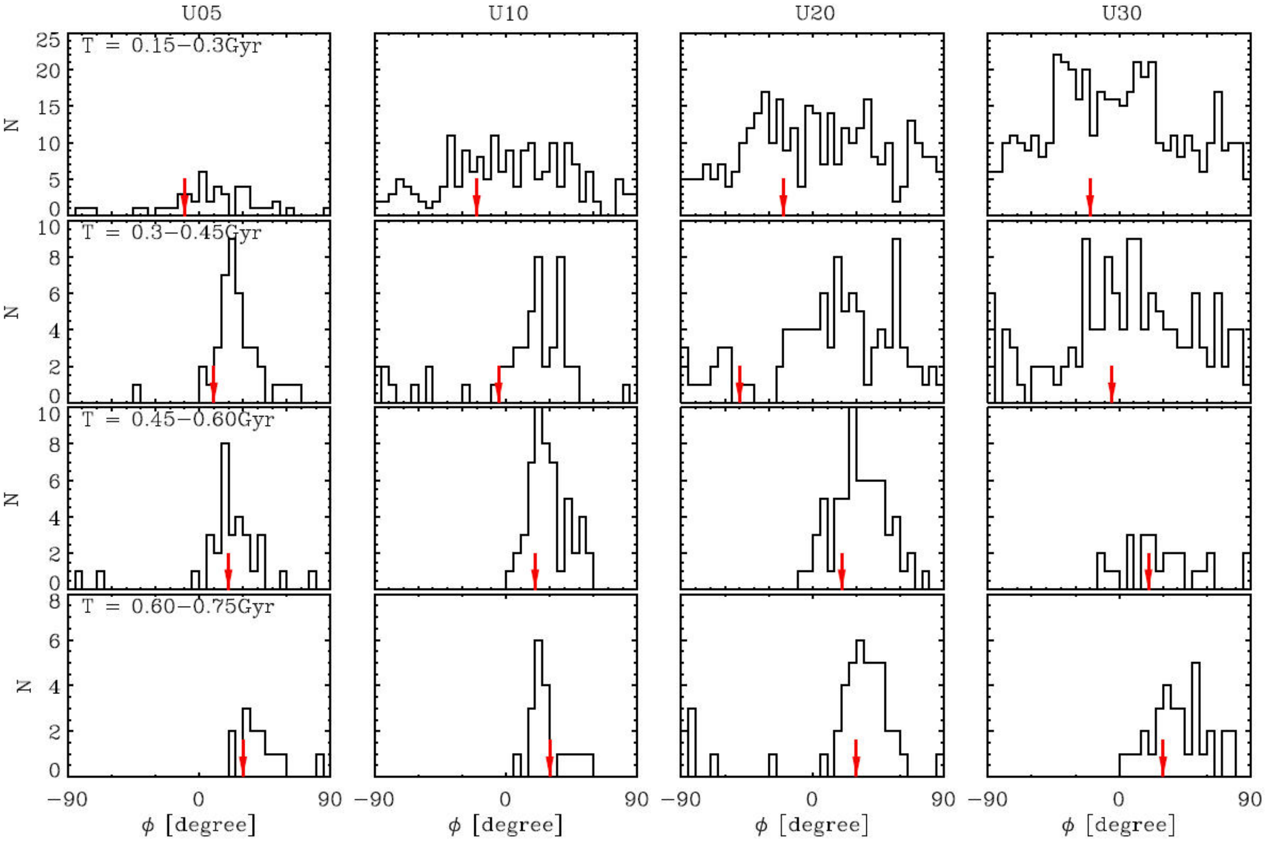

Figure 8. Histograms of the star clusters that formed in each selected time bin (with bin width of 0.15 Gyr) for all uniform-density models as a function of the azimuthal angle where they form. The arrow at the bottom of each panel indicates the mean position of a contact point.

SN feedback stirs the ring material vigorously, tending to increase density contrast between clumps and the background material. After the $\Sigma_{\rm SFR}$ peak, therefore, the total area covered by the gas with $\Sigma > 300$ M$_\odot$ pc^{-2} becomes smaller than before, resulting in larger $\Sigma_{\rm SFR}$.

Figure 7b plots the $\Sigma_{\rm SFR}$–$\overline{\Sigma}_{\rm cl}$ relationship measured at every 0.1 Gyr for (diamonds) the uniform-disk models and (asterisks) the exponential-disk models. Models with larger M_{x_1} tend to have larger $\Sigma_{\rm SFR}$ and larger $\overline{\Sigma}_{\rm cl}$. Note that our numerical results are overall consistent with the Kennicutt-Schmidt law for normal galaxies (squares) and circumnuclear starburst galaxies (pluses) adopted from Kennicutt (1998), and not much different from the observed $\Sigma_{\rm SFR}$–$\overline{\Sigma}_{\rm cl}$ relation for spatially-resolved star-forming regions (circles) in the nuclear ring of NGC 1097 taken from Hsieh et al. (2011).[4] There are large scatters in $\Sigma_{\rm SFR}$, amounting to $\sim$ 1–2 orders of magnitude, both in observational and simulation results. For star formation in nuclear rings of barred galaxies, the gas surface density probably sets the mean value of $\Sigma_{\rm SFR}$, as the Kennicutt-Schmidt law implies, while the scatters in $\Sigma_{\rm SFR}$ are likely due to the temporal variations of the mass inflow rate to the ring.

4. PROPERTIES OF STAR CLUSTERS AND GAS CLOUDS

4.1. *Azimuthal Age Gradient*

As mentioned in Introduction, observations indicate that some galaxies have well-defined azimuthal age gradients of star clusters in nuclear rings (e.g., Ryder et al. 2001; Allard et al. 2006; Böker et al. 2008; Ryder et al. 2010; van der Laan et al 2013), while others do not (e.g., Benedict et al. 2002; Brandle et al. 2012). Our simulations show that the presence or absence of the azimuthal age gradient is decided by the SFR in the ring (or, more fundamentally, on $\dot{M}_{\rm NR}$), independent of Σ_0 and the initial gas distribution.

Figure 8 plots for the uniform-density models the histograms of star clusters formed in each selected time bin, with bin width of 0.15 Gyr, as a function of the angular position where they form. The arrow at the bottom of each panel marks the location of a contact point that is moving in the positive azimuthal direction with time, as described in Section 3.1. Model U05 with $\Sigma_0 = 5$ M$_\odot$ yr^{-1} has SFR $\lesssim 0.1$ M$_\odot$ yr^{-1} (Fig. 4), and star-forming regions in this model are almost always localized to the contact point. In Models U20 and U30, on the other hand, star-forming regions are widely distributed along the azimuthal direction at early time ($t = 0.15 - 0.45$ Gyr) when SFR > 1 M$_\odot$ yr^{-1}, while they are preferentially found near the contact points at late time ($t \gtrsim 0.45$ Gyr) when SFR < 1 M$_\odot$ yr^{-1}.

Star clusters age as they orbit along the ring and emit copious UV radiations during about $\sim$ 10 Myr after birth. If star-forming regions are localized to the contact points, therefore, clusters would appear as "pearls

---

[4] In plotting the $\Sigma_{\rm SFR}$–Σ relation, Hsieh et al. (2011) used the maximum density of a cloud, instead of the mean density, for Σ.

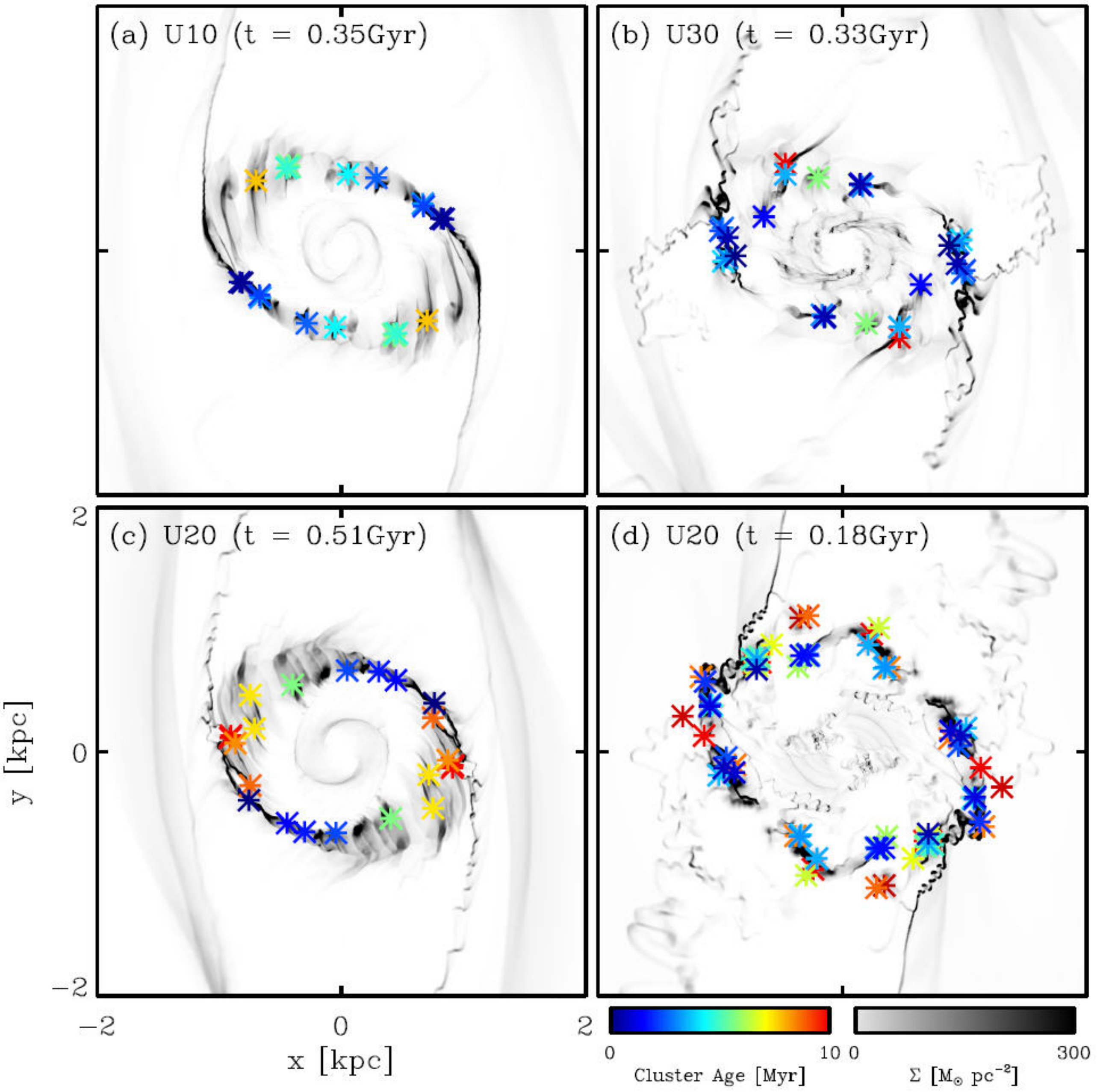

Figure 9. Positions and ages of young star clusters at selected epoches in Models U05, U20, and U30, overlaid on the gas density distribution in linear scale. The left panels show a clear azimuthal age gradient, while there is no age gradient in the right panels. Color indicates the cluster ages.

on a string" (e.g., Böker et al. 2008), with an age gradient along the rotational direction of the nuclear ring. This is illustrated in the left panels of Figure 9 which plot the spatial locations of star clusters with color indicating their ages (< 10 Myr), overlaid on the density distribution in linear scale, in Model U10 at $t = 0.35$ Gyr and Model U20 at $t = 0.51$ Gyr. There is clearly a positive bipolar age gradient starting from the contact points that are located at $\phi \sim 30^\circ$ and 210°. On the other hand, when the star-forming regions are randomly distributed throughout the ring, as in the "popcorn" model of Böker et al. (2008), star clusters with different ages would be mixed. In this case, there is no apparent age gradient along the ring, as exemplified in the right panels of Figure 9 for Model U30 $t = 0.33$ Gyr and Model U20 at $t = 0.18$ Gyr.

Why does then the SFR (or $\dot{M}_{\rm NR}$) matter for the azimuthal distributions of star-forming regions? The answer lies at the fact there is a limit on the rate of gas consumption at the contact points that occupy very small areas in the ring. When $\dot{M}_{\rm NR}$ is sufficiently small, most of the inflowing gas to the ring can be converted into stars at the contact points, and the resulting SFR is correspondingly small. When $\dot{M}_{\rm NR}$ is very large, on the other hand, the contact points cannot transform all the inflowing gas to stars instantaneously. The excess inflowing gas overflows the contact points and is transferred to other regions in the ring. The ring becomes denser not only by the addition of the overflowing gas but also by its own self-gravity. Some clumps in the ring achieve surface density above the threshold value, and start to form stars. We find that the rings have the Toomre stability parameter as low as ~ 0.5 when the SFR is near its peak, suggesting that gravitational instability promotes star formation.

Observations show that galaxies with no azimuthal age gradient have, on average, slightly larger SFRs in the rings (Mazzuca et al. 2008), although the spread in SFR for individual galaxies is too large to make this conclusive. Note, however, that the critical SFR determining the presence or absence of the azimuthal age gradient depends on many parameters. The maximum SFR at the contact points can be estimated as follows. Let Δr and $\Delta\phi$ denote the radial thickness and the azimuthal extent of a contact point, respectively. Then, the maximum SFR expected from two contact points is simply

$$\dot{M}_{*,\mathrm{CP}} = 2\epsilon_{\mathrm{ff}}\Sigma_{\mathrm{CP}} r_{\mathrm{NR}}\Delta r\Delta\phi/t_{\mathrm{ff}}, \tag{6}$$

where Σ_{CP} is the surface density of the contact points. The mean density of star-forming clouds is ~ 4000 M$_\odot$ pc^{-2}, which we take for Σ_{CP}. For $\epsilon_{\mathrm{ff}} = 0.01$, $\Delta r = 50$ pc, $\Delta\phi = 30°$, and $r_{\mathrm{NR}} = 1$ kpc typical in our models, equation (6) yields $\dot{M}_{*,\mathrm{CP}} \sim 1$ M$_\odot$ yr^{-1}, consistent with our numerical results. Note that the specific value of $\dot{M}_{*,\mathrm{CP}}$ depends on the parameters we adopt. In particular, $\dot{M}_{*,\mathrm{CP}} \propto c_s^3 r_{\mathrm{NR}}^2/R_{\mathrm{SF}}^{3/2}$ if the ring width is proportional to the ring radius, suggesting that galaxies with a weak bar (to have a smaller ring) and strong turbulence would have large $\dot{M}_{*,\mathrm{CP}}$.

4.2. *Radial Age Gradient*

Although the presence of an azimuthal age gradient depends on the SFR, we find that star clusters always display a radial age gradient. Figure 10 plots the spatial distributions of (left) the formation locations and (right) the present positions of star clusters on the x-y plane at $t = 1$ Gyr in Model U20. Each cluster is colored according to its formation time. The open circles denote the clusters that have passed the central region with $r < 0.3$ kpc at least once during their orbital motions: such clusters would have been destroyed at least partially by strong tidal fields near the galaxy center if their internal evolution such as core collapse, evaporation, disruption, etc. had been considered. On the other hand, the filled circles are for clusters that have never approached the central region, and thus are most likely to survive the galactic tide. The dashed lines draw the ring at $t = 1$ Gyr. Star-forming regions at late time are concentrated on the contact points, while they are well distributed at early time. Note that clusters that form early before the nuclear ring settles on an x_2-orbit have initial kick velocities quite different from those on x_1- or x_2-orbits at their formation locations. Although the ring soon takes on the x_2-orbit, these clusters move on eccentric orbits and wander around the nuclear region. Figure 10b shows that young clusters are preferentially found near the ring, while old clusters are located away from it, indicative of a positive radial gradient of their ages.

To show this more clearly, Figure 11 plots the age of clusters as functions of their present radial positions (circles) at $t = 1$ Gyr as well as their formation locations (plus symbols) for Models U10 and U20. Again, the open circles denote the clusters that have passed by the galaxy center, while the filled circles are for those that have not. Note that the age distributions of the present-day and formation-epoch locations of the clusters are not much different from each other, although the former shows a large spatial dispersion. The dispersion is larger for older clusters. To quantify the radial age gradient, we bin the clusters according to their ages, with a bin size of $\Delta\log(t/\mathrm{yr}) = 0.2$, and calculate the mean age and position in each bin. Our best fits of the ages to the formation-epoch positions are $\beta \equiv d\log(t/\mathrm{yr})/d(r/\mathrm{kpc}) \sim 14.4$ and 12.5 for Models U10 and U20, respectively. Column (7) of Table 2 gives β for all models. This radial age gradient results primarily from the decrease in the ring size with time, such that old clusters formed at larger galactocentric radii. Clusters diffuse out radially through gravitational interactions themselves and also with dense clouds in the ring, without much effect on the radial age gradient.

4.3. *Cluster Mass Functions*

Figure 12 plots the mass functions of all the clusters that have formed in each of the (left) uniform-disk and (right) exponential-disk models until $t = 1$ Gyr. The upper panels are for the clusters formed while star formation is very active with SFR ≥ 1 M$_\odot$ yr^{-1}, whereas those produced when SFR < 1 M$_\odot$ yr^{-1} are presented in the lower panels. In general, the mass distribution of clusters is described roughly by a power law, with its index depending on the SFR and M_{x_1}. When the SFR is larger than 1 M$_\odot$ yr^{-1}, the slope of the mass function is $\Gamma \equiv -d\log N/d\log M_* \sim 2$–3, with a smaller value corresponding to larger M_{x_1}. When SFR ≤ 1 M$_\odot$ yr^{-1}, clusters have a much steeper mass distribution with $\Gamma \gtrsim 3$. Column (8) of Table 2 gives Γ.

The dependence of the power-law index on the SFR and M_{x_1} can be understood as follows. When the SFR is large, there are numerous dense regions distributed throughout the ring. Such regions grow by accreting the surrounding material. Since star formation occurs in a stochastic manner in our models, some dense clouds have a chance to grow as massive as, or even larger than $\sim 10^7$ M$_\odot$, leading to a relatively shallow mass function. On the other hand, when the SFR is small, there are not many dense regions. Since the growth of density is quite slow in these models, they form stars at densities slightly above the critical value. In this case, most clusters have mass around $\sim 10^5 - 10^6$ M$_\odot$, with a steep mass distribution.

4.4. *Giant Clouds*

Finally, we present the properties of giant clouds located in nuclear rings. High-resolution radio observations show that nuclear rings consist of giant molecular associations at scale of ~ 0.2–0.3 kpc in which most star formation takes place. They typically have masses of $\sim 10^7$ M$_\odot$ and are gravitationally bound (e.g., Hsieh et al. 2011).

To identify giant clouds in our models, we utilize a core-finding technique developed by Gong & Ostriker (2011). This method makes use of the gravitational potential of

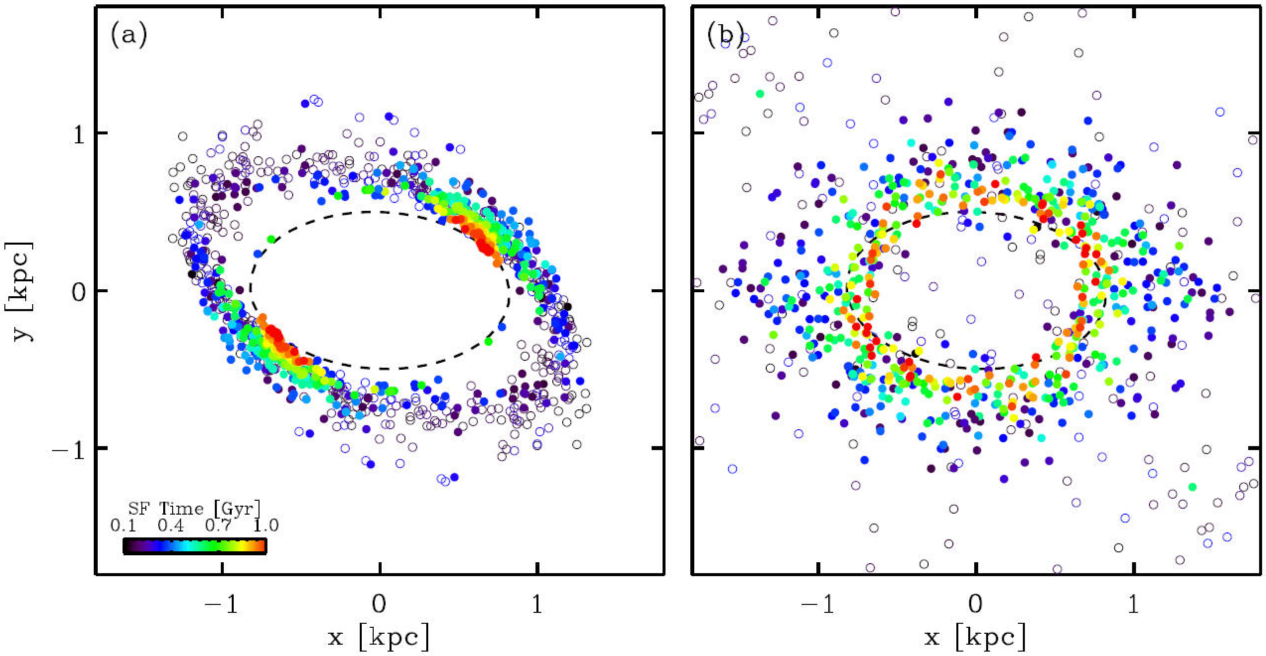

Figure 10. Spatial distributions of (a) the formation locations and (b) the present positions of star clusters in Model U20 at $t = 1$ Gyr. The dashed lines draw the ring at this time. Open circles denote the clusters that have passed the central region with $r < 0.3$ kpc during their orbits, while filled circles represent those that have not. Colorbar indicates the formation epoch of the clusters in unit of Gyr. At late time, stars form preferentially near the contact points. Gravitational interactions lead to diffusion of the clusters.

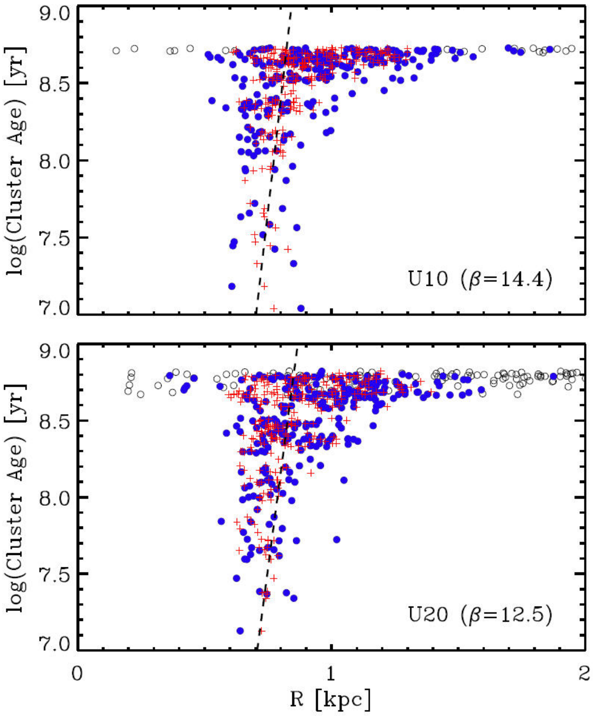

Figure 11. Ages of star clusters as functions of their current radial locations (circles) at $t = 1$ Gyr and their formation positions (pluses) for Models U10 and U20. Open circles are those that have passed by the galaxy center at a very close distance during orbital motions, while the filled circles are for those that have not. The dashed lines are the fits, with slopes of $\beta = d\log(t/\mathrm{yr})/d(r/\mathrm{kpc}) =$ 14.4 and 12.5, for the initial cluster positions, for Models U10 and U20, respectively.

the gas, and thus allows smoother cloud boundaries than the methods based on isodensity surfaces (see, e.g., Smith et al. 2009). At a given time, we search for all the local minima of the gravitational potential and find the largest closed potential contour encompassing one and only one potential minimum. We then define the potential minimum and outermost contour as the center and boundary of a cloud, respectively. If the distance between two neighboring minima is less than 0.1 kpc, we combine them. Figure 13 plots, for example, giant clouds identified by this technique for Model U20 at $t = 0.36$ Gyr. The left panel shows the gas surface density in linear scale, while the right panel displays boundaries of giant clouds as contours overlaid over the gravitational potential of the gas. A total of 14 giant clouds are identified. The mean values of their masses M, radii R, and one-dimensional velocity dispersions σ are 10^7 $\mathrm{M}_\odot$, 100 pc, and 20 km s^{-1}, respectively, corresponding to supersonic internal motions. The average density of the cloud boundaries is found to be ~ 300 $\mathrm{M}_\odot$ pc^{-2}. The average value of the virial parameter is $\alpha = 5\sigma^2 R/(GM) \sim 2$, so that they are gravitationally bound, consistent with the observed cloud properties in nuclear rings of barred galaxies (e.g., McKee & Ostriker 2007).

5. SUMMARY AND DISCUSSION

5.1. *Summary*

We have presented the results of two-dimensional hydrodynamic simulations of star formation occurring in nuclear rings of barred galaxies. We initially consider an infinitesimally thin, isothermal gas disk placed under the external gravitational potential. The external potential consists of a stellar disk, a stellar bulge, a central BH, and a non-axisymmetric stellar bar. We do not study the effect of spiral arms in the present work. The bar

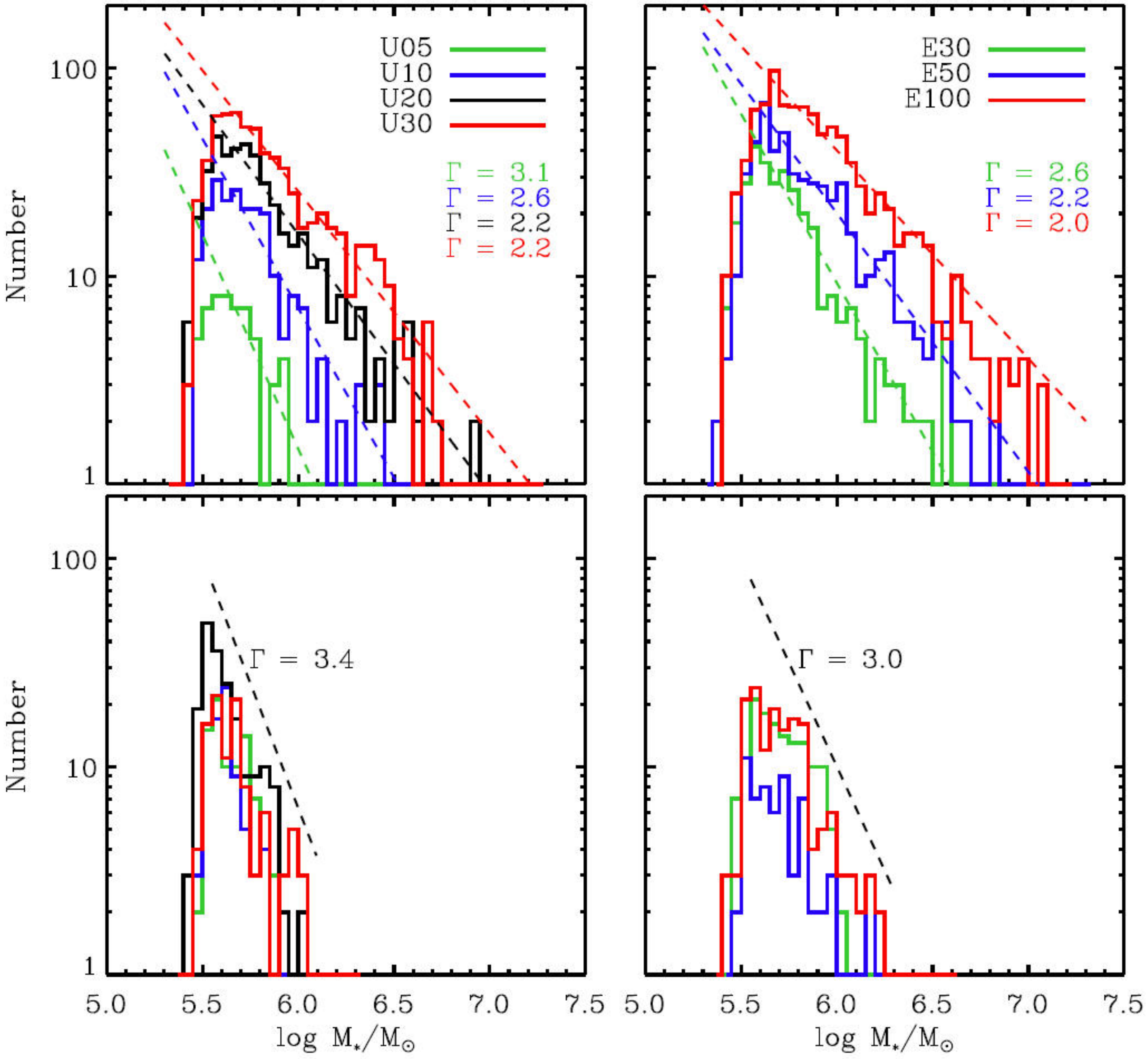

Figure 12. Clusters mass functions for (left) the uniform-density and (right) the exponential-density models. The upper and lower panels plot the clusters formed when the SFR is larger or smaller than 1 $M_\odot$ yr^{-1}, respectively. The mass function becomes shallower with increasing SFR.

potential is modeled by a Ferrers prolate spheroid with the semi-major and minor axes of 5 kpc and 2 kpc, respectively, and rotates about the galaxy center with a patten speed of 33 km s^{-1} kpc^{-1}. The bar mass, when it is fully turned on, is set to 30% of the total stellar mass in the spheroidal component, corresponding to a strongly barred galaxy. We fix the gas sound speed to $c_s = 10$ km s^{-1} and the BH mass to 4×10^7 $M_\odot$. Our simulations incorporate star formation recipes that include a density threshold corresponding to the Jeans condition, a star formation efficiency, conversion of gas to particles representing star clusters or their groups, and delayed momentum feedback via SN explosions. To explore various situations, we consider both uniform and exponential density models, and vary the gas surface density, bar growth time, and the total momentum injection in the in-plane direction. The main results of this work can be summarized as follows.

The imposed bar potential readily induces a pair of dust-lane shocks in the bar region inside the outermost x_1-orbit. At early time when the bar potential is weak, the dust-lane shocks are placed at the far downstream side from the bar major axis. As the bar potential increases, the dust-lane shocks become stronger and slowly move toward the bar major axis. The gas passing through the shocks loses a significant amount of angular momentum, infalls radially along the dust lanes, and forms a nuclear ring. The continuous gas inflows provide a fuel for star formation in the ring. After the bar potential reaches its full strength, the dust lanes settle on an x_1-orbit, while the nuclear ring follows an x_2-orbit. The remaining gas located inside the outermost x_1-orbit and outside the dust lanes is gathered to form an elongated inner ring in the bar region, whose shape is well described by an x_1-orbit, as well. Some of the gas located outside the outermost x_1-orbit transits to the inner ring

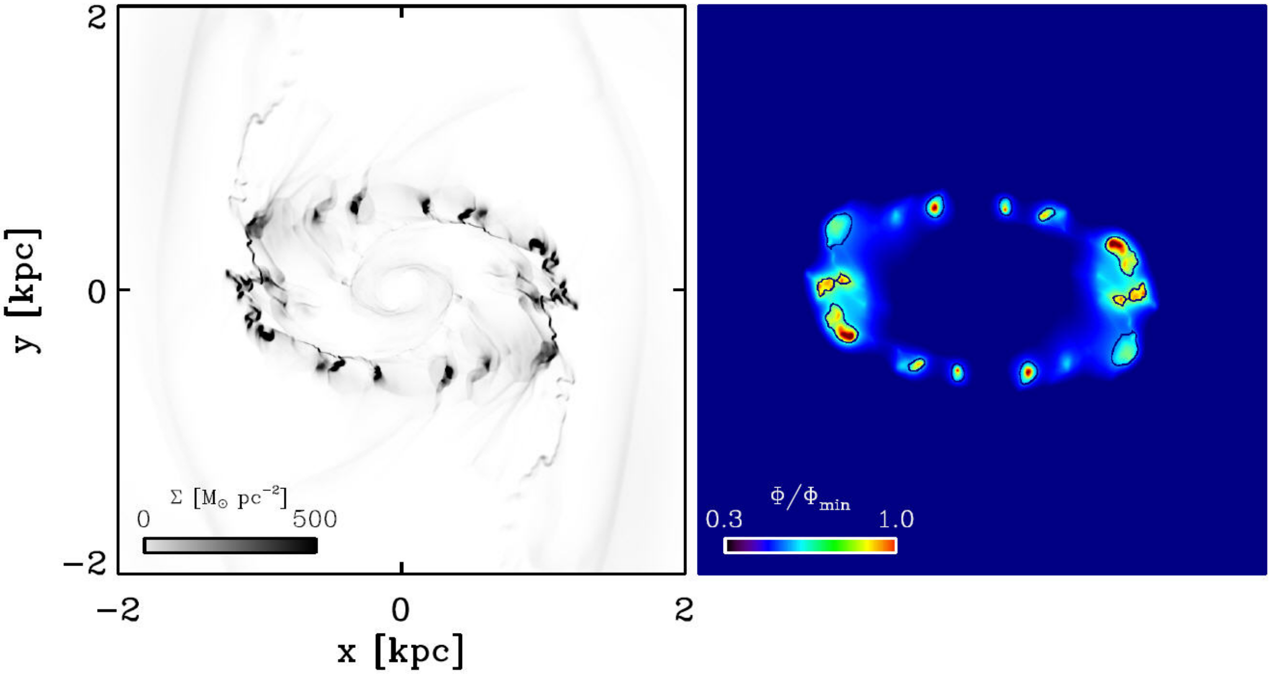

Figure 13. Distribution of giant clouds in the nuclear ring of Model U20 at $t = 0.36$ Gyr. Left: the gas surface density is shown in linear scale. Right: cloud boundaries found by the method described in the text are overlaid on the gravitational potential of the gas.

near the bar ends where x_1-orbits crowd. Similarly, the gas in the inner ring loses angular momentum when it collides with other gas near the bar ends, slowly infalling to the nuclear ring through the dust lanes.

The contact points between the dust lanes and the nuclear ring is a tunnel through which the inflowing gas on x_1-orbits switches to the x_2-orbit of the nuclear ring. About the time when the bar potential is fully turned on, the contact points are located near the bar minor axis. Over time, the nuclear ring shrinks in size due to the addition of low angular momentum gas from outside and by collisions of the ring material, which in turn makes the contact points rotate slowly in the counterclockwise direction. Since the contact points have largest density in the nuclear ring, they are preferred sites of star formation, although star-forming regions can be distributed throughout the ring when the mass inflow rate is high.

The bar potential transports the gas in the bar region to the nuclear ring very efficiently, but does not have strong influence on the gas orbits outside the bar region. This not only makes the bar region evacuated rapidly but also reduces the mass inflow rate $\dot{M}_{\rm NR}$ dramatically after ~ 0.3 Gyr. The SFR in nuclear rings displays a single primary burst followed by a few secondary bursts before becoming reduced to small values. The primary burst is associated with the massive gas inflow along the dust lanes caused by the growth of the bar potential. The duration and maximum rate of the primary burst depend on the growth time of the bar potential, in such a way that a slower bar growth results in a more prolonged and reduced SFR. The secondary bursts are due to the re-entry of the ejected and swept-up gas by SN feedback from the nuclear ring out to the bar-end regions. Time intervals between the secondary bursts are roughly $\sim 50-80$ Myr. The peak SFR is attained at $t \sim (0.8-1)\tau_{\rm bar}$, and the duration of active star formation is roughly a half of the bar growth time. The SFR is almost equal to $\dot{M}_{\rm NR}$. It has a weak dependence on the total gas mass $M_{\rm NR}$ in the ring when SFR $\gtrsim 1$ M$_\odot$ yr^{-1}, and is not correlated with $M_{\rm NR}$ when SFR $\lesssim 1$ M$_\odot$ yr^{-1}. This suggests that star formation in the ring is controlled primarily by $\dot{M}_{\rm NR}$ rather than $M_{\rm NR}$. The relationship between the SFR surface density and the surface density of dense clumps in nuclear rings found from our numerical models are consistent with the usual Kennicutt-Schmidt law for circumnuclear starburst galaxies.

The presence or absence of azimuthal age gradients of young star clusters in nuclear rings depends on the SFR (or $\dot{M}_{\rm NR}$) in our models. When $\dot{M}_{\rm NR}$ is small, most of the inflowing gas to the nuclear ring is consumed at the contact points. In this case, young star clusters that form would exhibit a well-defined azimuthal age gradient along the ring. When $\dot{M}_{\rm NR}$ is large, on the other hand, the contact points are unable to transform all of the inflowing gas to stars. The extra gas overflows the contact points and goes into the nuclear ring. The ring becomes massive and forms stars in clumps that become dense enough. In this case, no apparent age gradient of star clusters is expected since star-forming regions are randomly distributed over the whole length of the ring. The critical value of $\dot{M}_{\rm NR}$ that determines the presence or absence of the azimuthal age gradient is estimated to be ~ 1 M$_\odot$ yr^{-1} in our models, although it depends on various parameters such as the ring radius, critical density, etc. (eq. [6]).

Star clusters produced also exhibit a positive radial age gradient, such that young clusters are located close to the nuclear ring, while old clusters are found away from the ring. The primary reason for this is that the nuclear ring becomes smaller in size with time, and thus star-forming regions gradually move radially inward. In our models, the radial age gradient amounts to $\beta = d\log(t/\mathrm{yr})/d(r/\mathrm{kpc}) \sim 6-15$. Radial diffusion of clusters via mutual gravitational interactions and also with the gaseous ring does not affect the radial age gradient much.

When the SFR is large ($> 1\ \mathrm{M}_\odot\ \mathrm{yr}^{-1}$), some dense clouds are able to grow by accreting surrounding material and form massive clusters. The cluster mass function is well described by a power law, with slope $\Gamma = -d\log N/d\log M_* \sim 2-3$. A larger slope corresponds to a more massive disk in which more gas is available for the ring star formation. When the SFR is small, on the other hand, most clusters form near the threshold density, leading to a steeper slope with $\Gamma \gtrsim 3$. Giant clouds in nuclear rings have typical masses $10^7\ \mathrm{M}_\odot$ and sizes 0.1 kpc. Driven by momentum injection from SNe, their one-dimensional internal velocity dispersions are supersonic at $\sim 20\ \mathrm{km\ s}^{-1}$. They are gravitationally bound with the virial parameter of $\alpha \sim 2$.

5.2. *Discussion*

We find that the SFR in nuclear rings shows a strong primary burst, with its duration and peak value dependent on the bar growth time, and subsequently a few weak and narrow bursts, after which the SFR becomes very small. The peak of the primary burst is attained roughly when the bar potential is fully turned on. This burst behavior of the SFR appears to be a generic feature of star formation in nuclear rings of strongly-barred galaxies found in numerical simulations. For instance, N-body+ SPH models presented by Heller & Shlosman (1994), Knapen et al. (1995), and Friedli & Benz (1995) showed that the SFR reaches its peak value, with narrow bursts superimposed, about the time when the stellar bar fully develops, after which it is reduced to small values. In numerical modeling for star formation in the nuclear region of the Milky Way, Kim et al. (2011) found that the SFR is maximized at $t \sim 0.15$ Gyr, with a peak value $\sim 0.22\ \mathrm{M}_\odot\ \mathrm{yr}^{-1}$, and then drops to a relatively constant value $\sim 0.05-0.07\ \mathrm{M}_\odot\ \mathrm{yr}^{-1}$. The sustained star formation in Kim et al. (2011) is thought to arise because the Milky Way has a very weak bar that takes a long time to clear out gas in the bar region. In this case, the gas infall may proceed continuously over an extended period of time, a situation similar to the case with a slowly-growing bar.

There is observational evidence that star formation in nuclear rings occurs continually over a long period of time (a few Gyrs) with successive $\sim 4-10$ bursts separated by a few tenths of Gyrs each (e.g., Allard et al. 2006; Sarzi et al. 2007; see also van der Laan et al 2013). This is in sharp contrast to our numerical results that show that star formation in nuclear rings is dominated by one primary burst before declining to small values, with ~ 0.1 Gyr duration of active star formation. This discrepancy is mostly likely due to the fact that our models consider only a bar potential for angular momentum transport and thus are too simple to describe more complicated mass inflows in real disk galaxies. If the mass inflow rate to a nuclear ring really controls the SFR in the ring, as found by our numerical models, the observational results call for a need to feed the rings with gas episodically for a long time interval. *The bar potential alone is unlikely responsible for gas supply needed for star formation in real nuclear rings.* Unless bars are dynamically young, present star formation in nuclear rings of nearby barred galaxies requires additional gas feeding. One obvious such mechanism is spiral arms that can remove angular momentum at spiral shocks to transport gas from outer disks to the bar regions (e.g., Lubow et al. 1986; Kim & Stone 2012), which is not considered in the present work. Accretion of halo gas to the disk may not only rejuvenate bars (e.g., Bournaud & Combes 2002) but also enhance the SFR in the rings (e.g., Jiang & Binney 1999; Fraternali & Binney 2006, 2008). Such gas flows might actually exist, as evidenced by the presence of an enhanced number of carbon stars in the outer spiral arms of M33 (Block et al. 2007). Temporal variations in the bar strength (e.g., Bournaud & Combes 2002) and in the bar pattern speed (e..g, Combes & Sanders 1981) are also likely to affect the mass inflow rate to the ring and thus the SFR.

Some galaxies such as IC 4933 (Ryder et al. 2010) show age gradients of star clusters along the azimuthal direction in nuclear rings, while there are other galaxies such as NGC 7552 (Brandle et al. 2012) that do not show a clear age gradient. Mazzuca et al. (2008) analyzed Hα data for 22 nuclear rings and found that about half of their sample galaxies contain azimuthal age gradients, although most of them are not throughout the entire ring. They also found that the mean SFR in galaxies with azimuthal age gradients is $2.2 \pm 0.7\ \mathrm{M}_\odot\ \mathrm{yr}^{-1}$, which is slightly larger than the mean value of $3.6 \pm 1.1\ \mathrm{M}_\odot\ \mathrm{yr}^{-1}$ for galaxies with no apparent age gradient. While this appears consistent with our numerical results, the large dispersions in the mean SFRs suggest that there is no fixed SFR that can distinguish between galaxies with and without age gradients. In addition, the critical SFR for the absence or presence of azimuthal age gradients is about $1\ \mathrm{M}_\odot\ \mathrm{yr}^{-1}$ in our models, while most galaxies in the sample of Mazzuca et al. (2008) have SFR $> 1\ \mathrm{M}_\odot\ \mathrm{yr}^{-1}$. As equation (6) suggests for the maximum SFR, $\dot{M}_{*,\mathrm{CP}}$, allowed at the contact points, however, the critical SFR depends on many factors that may vary from galaxy to galaxy. For example, NGC 1343 with the most clear bi-polar age gradient in the Mazzuca et al. (2008) sample has the current SFR of $\sim 6.8\ \mathrm{M}_\odot\ \mathrm{yr}^{-1}$. Its ring radius is ~ 2 kpc (Comerón et al. 2010), which increases the critical SFR by a factor of 4, assuming that the ring width is proportional to the ring size and the other parameters remain the same. In addition, $\dot{M}_{*,\mathrm{CP}} \propto \Sigma_{\mathrm{CP}}^{3/2} \propto c_s^3/R_{\mathrm{SF}}^{3/2}$, so that the level of interstellar turbulence and the size of star-forming regions R_{SF} may change $\dot{M}_{*,\mathrm{CP}}$ considerably.

We find that star clusters that form in nuclear rings naturally develop a positive radial gradient of their ages owing primarily to the decrease in the ring size over $\sim$ Gyr in our models. This is consistent with the results of Jang & Lee (2013) who found that clusters with ages $\lesssim 1$ Gyr in the nuclear region of NGC 1672 are older systematically with increasing radius. Note that the radial age gradient holds over a timescale of $\sim$ Gyr and may not apply to clusters in a small age range since the decay of the ring size is quite slow. Indeed, Mazzuca et al. (2008) found that two (NGC 5953 and 7570) of their sample galaxies show a negative radial age gradient of H II regions in the rings.[5] Our numerical results plotted in Figure 11 also show that when limited to clusters with age $\sim 10^7$–$10^{7.5}$ yr at $t = 1$ Gyr, younger clusters can be found at larger radii, which is due to the stochastic nature of star formation and ensuing gravitational interactions.

Our results show that the SFR in the nuclear rings is tightly correlated with the mass inflow rate to the ring rather than the total gas mass in the ring (Fig. 6). This result is seemingly consistent with the results of Benedict et al. (2002) who found that the SFR in the nuclear ring of a strongly-barred galaxy NGC 4314 is smaller, by a factor of 30, than that in a weakly-barred galaxy NGC 1326 (Buta et al. 2000), even if the gas mass in the ring is smaller by only a factor of two. It is interesting to note that the gas mass contained in most "gas-rich" nuclear rings of barred galaxies in the BIMA SONG sample is in a remarkably narrow range of $\sim (1-6) \times 10^8$ $M_\odot$ (Sheth et al. 2005).[6] The SFR data presented in Mazzuca et al. (2008) combined with the bar strength given in Comerón et al. (2010) show that strongly-barred galaxies usually have very small present-day SFRs and the SFRs in weakly-barred galaxies vary in a wide range, although the number of galaxies in their sample is too limited to make a conclusive statement. It will be interesting to see how the bar strength as well as gas inflows by spiral shocks influence the SFR in nuclear rings.

While star formation is concentrated in nuclear rings in our models, observations indicate that star formation in some galaxies occurs not only in nuclear rings but also in the bar region including dust lanes (e.g., Martin & Friedli 1997; Sheth et al. 2000; Zurita & Pérez 2008; Elmegreen et al. 2009; Martínez-García & González-Lópezlira 2011). While dust lanes themselves are known hostile to star formation due to strong velocity shear (e.g., Athanassoula 1992; Kim et al. 2012a), Sheth et al. (2000) proposed that stars form in interbar dust spurs in filamentary shape that impact the dust lanes from the trailing side of the bar (see also Sheth et al. 2002; Zurita & Pérez 2008). Indeed, Elmegreen et al. (2009) inferred that some clusters in the nuclear ring of NGC 1365 actually formed in one of the dust lanes by the impact of spurs and subsequently migrated inward to the nuclear ring. The origin of these interbar spurs is yet unclear. Apparently, there is no filamentary interbar feature in our models. They may originate from gas inflows due to spiral shocks from the region outside the bar (Elmegreen et al. 2009), from interactions of gas with magnetic fields that are pervasive in the bar region (Beck et al. 1999, 2005), and/or from other dynamical processes that involve gas cooling, self-gravity, etc., which are not considered in the present work. It will be an important direction of future work to study how spiral arms and magnetic fields affect the gas inflows and star formation in the bar and nuclear regions.

We gratefully acknowledge I. S. Jang and M. G. Lee for sharing their results on the radial age gradient of clusters found in NGC 1672. We also thank E. C. Ostriker and K. Sheth for helpful discussions, and are grateful to the referees for an insightful report and for the information on ESO 565-11. This work was supported by the National Research Foundation of Korea (NRF) grant funded by the Korean government (MEST), No. 2010-0000712. The computation of this work was supported by the Supercomputing Center/Korea Institute of Science and Technology Information with supercomputing resources including technical support (KSC-2012-C3-19).

REFERENCES

Allard, E. L., Knapen, J. H., Peletier, R. F., & Sarzi, M. 2006, MNRAS, 371, 1087

Ann, H. B., & Thakur, P. 2005, ApJ, 620, 197

Athanassoula, E. 1992, MNRAS, 259, 345

Beck, R., Ehle, M., Shoutenkov, V., Shukurov, A., Sokoloff, D. 1999, Nature, 397, 324

Beck, R., Fletcher, A., Shukurov, A., Snodin, A., Sokoloff, D. D., Ehle, M., Moss, D., & Shoutenkov, V. 2005, A&A, 444, 739

Benedict, G. F., Howell, D. A., Jørgensen, I., Kenney, J. D. P., & Smith, B. J. 2002, AJ, 123, 1411

Block, D. L., Combes, F., Puerari, I., et al. 2007, A&A, 471, 467

Böker, T., Falcón-Barroso, J., Schinnerer, E., Knapen, J. H., & Ryder, S. 2008, AJ, 135, 479

Bournaud, F. & Combes, F. 2002, A&A, 392, 83

Brandl, B. R., Martín-Hernández, N. L., Schaerer, D., Rosenberg, M., & van der Werf, P. P. 2012, A&A, 543, A61

Burbidge, E. M., & Burbidge, G. R. 1960, ApJ, 132, 30

Buta, R. 1986, ApJS, 61, 609

Buta, R., & Combes, F. 1996, Fund. Cosmic Phys., 17, 95

Buta, R., Crocker, D. A., & Byrd, G. G. 1999, AJ, 118, 2071

Buta, R., Treuthardt, P. M., Byrd, G. G., & Crocker, D. A. 2000, AJ, 120, 1289

Chevalier, R. A. 1974, ApJ, 188, 501

Cioffi, D. F., McKee, C. F., & Bertschinger, E. 1988, ApJ, 334, 252

Combes F. 2001, in Aretxaga I., Kunth D., Mújica R., eds, Advanced Lectures on the Starburst-AGN (World Scientific: Singapore), p223

Combes F., & Gerin M. 1985, A&A, 150, 327

Combes, F., & Sanders, R. H. 1981, A&A, 96, 164

Comerón, S., Martínez-Valpuesta, I., Knapen, J. H., Beckman, J. E. 2009, ApJ, 706, L256

Comerón, S., Knapen, J. H., Beckman, J. E., Laurikainen, E., Salo, H., Martínez-Valpuesta, & Buta, R. J. 2010, MNRAS, 402, 2462

Dobbs, C. L., & Pringle, J. E. 2010, MNRAS, 409, 396

Elmegreen, B. G. 1994, ApJ, 425, 73

Elmegreen, B. G., Galliano, E., & Alloin, D. 2009, ApJ, 703, 1297

Englmaier, P., & Gerhard, O. 1997, MNRAS, 287, 57

Ferrers, N. M. 1887, Q. J. Pure Appl. Math., 14, 1

Field, G. B. 1965, ApJ, 142, 531

Fraternali F., Binney J. 2006, MNRAS, 366, 449

Fraternali F., Binney J., 2008, MNRAS, 386, 935

Friedli, D. & Benz, W. 1995, A&A, 301, 649

Gong, H., & Ostriker, E. C. 2011, ApJ, 729, 120

Heger, A., Fryer, C. L., Woosley, S. E., Langer, N., & Hartmann, D. H. 2003, ApJ, 591, 288

Heller, C. H., & Shlosman, I. 1994, ApJ, 424, 84

Hockney, R. W., & Eastwood, J. W. 1988, Computer Simulation Using Particles (Philadelphia: Adam Hilger)

Hopkins, P. F., Quataert, E., & Murray, N. 2011, MNRAS, 417, 950

Hsieh, P.-Y., Matsushita, S., Liu, G. Ho, P. T. P., Oi, N., & Wu, Y.-L. 2011, ApJ, 736, 129

Jang, I. S., & Lee, M.-G. 2013, in preparation

Jiang, I.-G., & Binney, J. 1999, MNRAS, 303, L7

Kalnajs, A. J. 1971, ApJ, 166, 275

Kennicutt, R. C., Jr. 1998, ApJ, 498, 541

Knapen J. H., Beckman J. E., Heller C. H., Shlosman I., de Jong R. S. 1995, ApJ, 454, 623

Knapen, J. H., Mazzuca, L. M., Böker, T., Shlosman, I., Colina, L., Combes, F., & Axon, D. J. 2006, A&A, 448, 489

Kenney, J. D. P., Wilson, C. D., Scoville, N. Z., Devereux, N. A., & Young, J. S. 1992, ApJ, 395, 79

---

[5] Note that NGC 5953 is a non-barred galaxy.

[6] While Sheth et al. (2005) reported that the ring in NGC 6946 has a mass of $\sim 10^9$ $M_\odot$, a higher-resolution observation of Schinnerer et al. (2006) gives the ring mass of $\sim 4 \times 10^8$ $M_\odot$.

Kim, C.-G., Kim, W.-T., & Ostriker, E. C. 2006, ApJ, 649, L16
Kim, C.-G., Kim, W.-T., & Ostriker, E. C. 2010, ApJ, 720, 1454
Kim, C.-G., Kim, W.-T., & Ostriker, E. C. 2011, ApJ, 743, 25
Kim, S. S., Saitoh, T. R., Jeon, M., et al. 2011, ApJ, 735, L11
Kim, W.-T., & Ostriker, E. C. 2006, ApJ, 646, 213
Kim, W.-T., & Stone, J. M. 2012, ApJ, 751, 124
Kim, W.-T., Seo, W.-Y., Stone, J. M., Yoon, D., & Teuben, P. J. 2012a, ApJ, 747, 60
Kim, W.-T., Seo, W.-Y., & Kim, Y. 2012b, ApJ, 758, 14 (Paper I)
Kohno, K., Kawabe, R., & Vila-Vilaró, B. 1999, ApJ, 511, 157
Kroupa, P. 2001, MNRAS, 322, 231
Krumholz, M. R., McKee, C. F. 2005, ApJ, 630, 250
Krumholz, M. R., & Tan, J. C. 2007, ApJ, 654, 304
Lee, E., & Goodman, J. 1999, MNRAS, 308, 984
Lejeune, T., & Schaerer, D. 2001, å, 366, 538
Lubow, S. H., Balbus, S. A., & Cowie, L. L. 1986, ApJ, 309, 496
Maciejewski, W., Teuben, P. J., Sparke, L. S., & Stone, J. M. 2002, MNRAS, 329, 502
Maoz, D., Barth, A. J., Ho, L. C., Sternberg, A., & Filippenko, A. V. 2001, AJ, 121, 3048
Martin, P., & Friedli, D. A&A, 1997, 326, 449
Martini, P., Regan, M. R., Mulchaey, J. S., & Pogge, R. W. 2003, ApJ, 589, 774
Martínez-García, E. E., González-Lópezlira, R. A. 2011, ApJ, 734, 122
Mazzuca, L. M., Knapen, J. H., Veilleux, S., & Regan, M. W. 2008, ApJ, 174, 337
Mazzuca, L. M., Swaters, R. A., Knapen, J. H., & Veilleux, S. 2011, ApJ, 739, 104
McKee, C. F., Ostriker, E. C. 2007, ARA&A, 45, 567
Ostriker, E. C., McKee, C. F., & Leroy, A. K. 2010, ApJ, 721, 975
Ostriker, E. C., & Shetty, R. 2011, ApJ, 731, 41
Patsis, P. A., & Athanassoula, E. 2000, A&A, 358, 45
Peeples, M. S., & Martini, P. 2006, ApJ, 652, 1097
Phillips, A. C. 1996, in ASP Conf. Ser. 91, Barred Galaxies, ed. R. Buta, D. A. Crocker, & B. G. Elmegreen (San Francisco: ASP), 44
Piner, B. G., Stone, J. M., & Teuben, P. J. 1995, ApJ, 449, 508
Portegies Zwart S. F., McMillan S. L. W., & Gieles, M. 2010, ARA&A, 48, 431
Regan, M. W., & Teuben, P. J. 2003, ApJ, 582, 723
Regan, M. W., & Teuben, P. J. 2004, ApJ, 600, 595
Regan, M. W., Sheth, K., Teuben, P. J., & Vogel, S. N. 2001, ApJ, 574, 126
Ryder, S. D., Knapen, J. H. & Takamiya, M. 2001, MNRAS, 323, 663
Ryder, S. D., Illingworth, S. M., Sharp, R. G., & Farage, C. L. 2010, PASA, 27, 56
Reynaud, D., & Downes, D. 1997, A&A, 319, 737
Sandage, A. R. 1961, The Hubble Atlas of Galaxies (Washington, DC: Carnegie Institution of Washington)
Sanders, R. H., & Huntley, J. M. 1976, ApJ, 209, 53
Sandstrom, K., Krause, O., Linz, H., Schinnerer E. et al. 2010, A&A, 518, L59
Sarzi, M., Allard, E. L, Knapen, J. H., & Mazzuca, L. M. 2007, MNRAS, 380, 949
Schinnerer, E., Böker, T., Emsellem, E., & Lisenfeld, U. 2006, ApJ, 649, 181
Schmidt, M. 1959, ApJ, 129, 543
Sheth, K., Regan, M. W., Vogel, S. N., & Teuben, P. J. 2000, ApJ, 532, 221
Sheth, K., Vogel, S. N., Regan, M. W., Teuben, P. J., & Harris, A. I. 2000, AJ, 124, 2581
Sheth, K., Vogel, S. N., Regan, M. W. et al. 2005, ApJ, 632, 217
Shetty, R., & Ostriker, E. C. 2008, ApJ, 684, 978
Shetty, R., & Ostriker, E. C. 2012, ApJ, 754, 2
Shlosman, I., Begelman, M. C., & Frank, J. 1990, Nature, 345, 679
Shull, J. M. 1980, ApJ, 237, 769
Smith, R. J., Clark, P. C., & Bonnell, I. A. 2009, MNRAS, 396, 830
Thakur, P., Ann, H. B., & Jiang, I. 2009, ApJ, 693, 586
van der Laan, T. P. R., Schinnerer, E., Emsellem, E., et al. 2013, accepted for publication in A&A; arXiv:1301.2621
van de Ven, G., & Chang, P. 2009, ApJ, 697, 619
Williams, J. P., Blitz, L., & McKee, C. F. 2000, in Protostars and Planets IV, ed. V. Mannings, A. P. Boss, & S. S. Russell (Tuscon: Univ. Arizona Press), 97
Wolfire, M. G., McKee, C. F., Hollenbach, D., & Tielens, A. G. G. M. 2003, ApJ, 587, 278
Zurita, A., & Pérez, I. 2008, A&A, 485, 5